

New Signal and Algorithms for 5G/6G High Precision Train Positioning in Tunnel with Leaky Coaxial Cable

Lu Yin, *Member, IEEE*, Tianzhu Song, Qiang Ni, *Senior Member, IEEE*, Quanbin Xiao, Yuan Sun, Wenfang Guo

Abstract—High precision train positioning is a crucial component of intelligent transportation systems. Tunnels are commonly encountered in subways and mountainous regions. As part of the communication system infrastructure, Leaky Coaxial (LCX) Cable is widely equipped as antenna in tunnels with many advantages. LCX positioning holds great promise as a technology for rail applications in the upcoming B5G (beyond-5G) and 6G eras. This paper focuses on the LCX positioning methodology and proposes two novel algorithms along with a novel communication-positioning integration signal. Firstly, a novel algorithm called Multiple Slot Distinction (MSD) LCX positioning algorithm is proposed. The algorithm utilizes a generated pseudo spectrum to fully utilize the coupled signals radiated from different slots of LCX. This approach offers higher time resolution compared to traditional methods. To further improve the positioning accuracy to centimeter-level and increase the measuring frequency for fast trains, a novel communication-positioning integration signal is designed. It consists of traditional Positioning Reference Signal (PRS) and a significantly low power Fine Ranging Signal (FRS). FRS is configured to be continuous and superposed onto the cellular signal using Non-Orthogonal Multiple Access (NOMA) principle to minimize its interference to communication. A two-stage LCX positioning method is then executed: At the first stage, the closest slot between the receiver and LCX is estimated by the proposed MSD algorithm using PRS; At the second stage, centimeter-level positioning is achieved by tracking the carrier phase of the continuous FRS. This process is assisted by the closest slot estimation, which helps mitigate interference between neighboring slots and eliminate the integer ambiguities. Simulation results show our proposed LCX position methodology outperforms the existing ones and offer great potentials for future implementations.

Index Terms—Train Positioning, 5G/6G, leaky coaxial cable, fine ranging signal, non-orthogonal multiple access.

I. INTRODUCTION

SMART rail is an important part of intelligent transportation system, with high precision positioning services as its foundation. The widely used balise and cross inductive loop provide precise positions only when the train passes them [1],

This research was supported in part by the Key Research and Development Program of China under Grant 2022YFB2601801, in part by the Beijing Municipal Natural Science Foundation under Grant L191003, and in part by the State Key Laboratory of Information Photonics and Optical Communications (BUPT) under Grant IPOC2023ZT01 (Corresponding author: Lu Yin.)

Lu Yin, Tianzhu Song, Quanbin Xiao, Yuan Sun and Wenfang Guo are with the School of Electronic Engineering, Beijing University of Posts and Telecommunications, Beijing, 100876, China, e-mail: inlu_mail@bupt.edu.cn, stztc112358@bupt.edu.cn, xiaoquanbin@bupt.edu.cn, sunyuan@bupt.edu.cn, guowenfang@bupt.edu.cn.

Qiang Ni is with the School of Computing and Communications, Lancaster University, InfoLab21, LA1 4WA, U.K. e-mail: q.ni@lancaster.ac.uk.

[2]. Tachometer equipped on trains cannot output absolute positions and are prone to accumulative errors [3]. Global Navigation Satellite System (GNSS) can provide continuous absolute positions with accuracy of meter level. It can even achieve centimeter-level accuracy if enhanced by RTK (Real-time kinematic) or 5G systems [4], [5]. However, GNSS is easily blocked which makes it unavailable in undergrounds or tunnels.

Leaky Coaxial (LCX) cable is a type of antenna that radiates and receives electromagnetic waves through a series of dense slots cut on its outer conductor layer. It is widely employed in tunnels as it offers advantages such as easy installation, uniform coverage and reduced inter-cell interference [6]. It is an effective way to broadcast positioning signal through LCX in tunnels to overcome the coverage problem. Theoretically, LCX could broadcast any wireless signals (including GNSS-like signal, communication signal, etc.) within its bandwidth. In practical applications, 5G networks provide the native support for positioning and have the potential to outperform GNSS due to the wider bandwidth, stronger power, denser network, etc [7], [8], [9]. Furthermore, since LCX is typically installed for communication systems, utilizing communication signals for positioning via LCX offers additional benefits in terms of performance, cost and multi-system maintenance considerations.

In industry, the 3rd Generation Partnership Project (3GPP) has given the requirements for train positioning both outdoor and in tunnels at the latest release [10]. Although there are studies that have studied 5G train positioning using ordinary antennas [11], [12], [13], there remains a lack of research focusing on positioning via LCX, which is insufficient to meet the current and future requirements for the rail use cases.

The LCX positioning can be classified into the fingerprint-based method and time-based method. Received Signal Strength Indicator (RSSI) or Channel State Information (CSI) is adopted as the fingerprint features to identify the positions by comparing the different feature patterns before and after a train passes [14], [15], [16]. In time-based methods, [17] proposes a Time-of-Arrival (TOA)-based LCX positioning method by using both the direct wave and the reflected wave from the end of LCX. But it is under the assumption of perfect time synchronization between Base Station (BS) and receiver, which is hardly implemented in practical uses. An additional BS is placed at the end of LCX to avoid the impact of imperfect time synchronization and high propagation loss of the reflected signal in [18]. The MULTiple-Signal-Classification

(MUSIC)-based LCX positioning methods treat the frequency samples as the antenna array elements in conventional MUSIC. Then, a pseudo spectrum is generated by using steering vectors with different time delays and the noise sub-spaces decomposed from the received signal to estimate the time delay of signal [19], [20], [21]. However, the signals radiated from different slots on LCX couple to each other [22], [23]. The interference between the slots will cause signal distortion at the receiver side. Because MUSIC requires the coexistent sources to be uncorrelated, it cannot properly differentiate the signals from neighboring slots, leading to a low time domain resolution. Meanwhile, the positioning signals used in current researches are PRS-like¹, which must be broadcasted in a small amount of time slots to avoid occupying too many communication resources [24], [25]. This not only limits its ranging accuracy as the intermittent signal is hardly tracked, but also leads to low measuring frequency because of the long interval between two positioning frames, which cannot meet the accuracy and real-time requirements of fast train positioning [10], [26]. Although higher positioning accuracy could be achieved by placing two LCXs perpendicular to each other [27], it cannot be implemented in tunnels.

To tackle the above problems, we aim to develop a brand new centimeter-level two-stage LCX positioning methodology with the design of a novel signal waveform to meet the future requirements for the rail use cases in the upcoming B5G (beyond-5G) and 6G eras. To the best of our knowledge, there is little comprehensive research on the LCX positioning from signal to algorithm level which makes our work very challenging. The main contributions of this paper are:

- 1) We propose a novel Multiple Slot Distinction (MSD) algorithm for LCX positioning. Different from the traditional MUSIC-based algorithm, which estimates time delay based on the orthogonal relationship between signal and noise sub-spaces in frequency domain, the position is estimated directly in MSD algorithm by searching for the peak of a position-related pseudo spectrum with high time resolution. This pseudo spectrum is generated by the revealed relationship between the receiver's position and the coupled signals in time domain.
- 2) We design a novel communication-positioning integration signal that is highly compatible with the 5G/6G system to achieve a centimeter-level ranging capability without interfering communication much. A full-power PRS along with a significantly low power positioning waveform, called Fine Ranging Signal (FRS), works together to realize a two-stage positioning. Both PRS and FRS could be configured within the 3GPP framework. PRS is employed as a pilot to estimate the closest slot between LCX and receiver through MSD algorithm. FRS is continuous and superposed upon the cellular signal² based on the Non-Orthogonal Multiple Access (NOMA)

¹PRS stands for the Positioning Reference Signal in 4G and 5G systems.

²The cellular signal is the same as the communication signal mentioned above. To avoid confusion, we use cellular signal to represent the PRS and the signal for communication purpose, which is denoted as Communication Signal (CS), from now on.

principle to minimize its interference to communication. Then, a centimeter-level LCX positioning method is developed by tracking the carrier phase of FRS with the help of the closest slot estimation to reduce the interference between neighboring slots and eliminate the integer ambiguities.

- 3) A series of analyses are done to evaluate the performance of the proposed LCX positioning methodology. The results show our proposed two-stage LCX positioning method along with the novel PRS+FRS waveform has a great improvement of ranging/positioning accuracy than traditional methods. Furthermore, FRS causes a negligible Bit Error Rate (BER) loss, indicating that FRS causes little interference to CS.
- 4) The potential of the proposed LCX positioning methodology with redundant infrastructure is explored. The system is expanded to a dual-LCX setup. Analysis and simulations show that the redundant infrastructure can improve the positioning accuracy and robustness of the system, while allowing for 2-Dimensional (2D) positioning ability. The redundant infrastructure can offer valuable implications for various scenarios.

The rest of this paper is organized as follows: Section II gives the background knowledge of LCX and a typical LCX positioning scenario. Section III proposes the MSD algorithm for LCX positioning. Section IV describes the proposed two-stage LCX positioning method in detail by designing a novel communication-positioning integration signal and introducing a carrier phase integer ambiguity elimination algorithm. Section V evaluates the performance of the proposed methodology. Section VI discusses the proposed methodology's performance potential with redundant infrastructure. Finally, the conclusions are given in Section VII.

II. PRELIMINARY

A. The properties of LCX

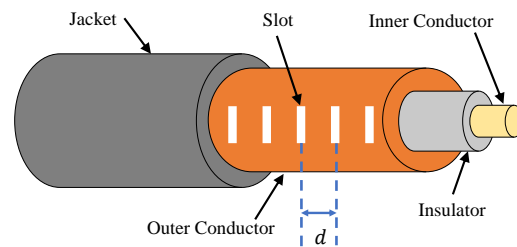


Fig. 1. The Structure of LCX.

Slots are cut on the outer conductor of an LCX as Fig.1 shows. The slots are often arranged periodically with a distance of d , allowing for the leakage of surface and radiated waves. A small portion of the transmitted energy will be taken by the radiated wave from each slot. The inclined angles of the slots affect the electric field distributions around LCX. Vertical slots are used in this paper because there is only electric field in longitudinal direction. Other cases can be studied in the same way by decomposing electric fields into different directions [22]. Then, the electric field around LCX can be considered as

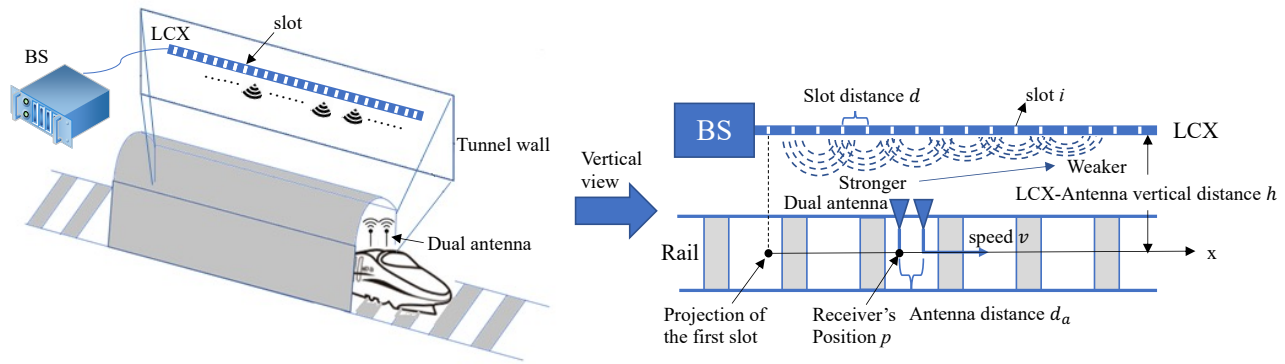


Fig. 2. A typical 5G/6G LCX positioning scenario.

the superposition of a series of magnetic dipoles that represents each slot, which can be expressed as [23]:

$$E = \sum_{i=1}^M E^{(i)} = \sum_{i=1}^M E_0^{(i)} \frac{e^{-jKr^{(i)}}}{r^{(i)}} \sin(\theta^{(i)}) \quad (1)$$

where M is the amount of slots. $E^{(i)}$ is the electric field distribution at slot i with the intensity of $E_0^{(i)}$. $r^{(i)}$ and $\theta^{(i)}$ are the distance and angle between the field point and the center of slot i , respectively. $K = 2\pi f/c$ is the propagation constant of electromagnetic wave in free space, where f and c are the electric wave frequency and the speed of light, respectively. Define $\alpha^{(i)}$ and $\beta^{(i)}$ as the amplitude attenuation and the phase variation of the electric field intensity at the center of slot i , respectively. Then, the electric field intensity is:

$$E_0^{(i)} = E_0 \cdot \alpha^{(i)} \cdot e^{-j\beta^{(i)}} \quad (2)$$

where $E_0 = E_0^{(1)}$ is the electric field intensity at the first slot. The amplitude attenuation is related to the LCX's longitudinal attenuation constant (α_0 in dB/100m) and the path distance as:

$$\alpha^{(i)} = 10^{-\frac{(\frac{\alpha_0}{100} \times d(i-1))}{20}} = 10^{-\frac{\alpha_0 d(i-1)}{2000}} \quad (3)$$

The phase variation is related to the path distance and the LCX's propagation constant K_r , which, in turn, is determined by the material of LCX. The phase variation is expressed as:

$$\beta^{(i)} = K_r d(i-1) = K \sqrt{\varepsilon_r} d(i-1) \quad (4)$$

where ε_r is the LCX's relative permittivity. Please notice that there are two types of propagation constant: one (K) is for the wireless channel, the other (K_r) is for the wired channel in LCX.

B. LCX positioning scenario

Consider a typical 5G/6G LCX positioning scenario for train positioning as Fig.2 shows. An LCX is placed parallel to the straight rail at a distance of h , on which M slots are cut with the slot spacing of d between their centers. BS is placed on the

start/end of LCX to transmit communication and positioning signals. The train is running with a speed of v . Define the projection of the first slot on the rail track as the origin. The receiver at position p is equipped with dual antennas located at $p_1 = p$ and $p_2 = p + d_a$, respectively. The dual antenna is used to eliminate the geometric ambiguity explained in Section IV-C. The antenna and LCX are assumed at the same heights.

III. THE PROPOSED MULTIPLE SLOT DISTINCTION ALGORITHM

In this section, a novel Multiple Slot Distinction (MSD) algorithm is proposed to estimate the train position. Firstly, we construct a position-based LCX channel matrix. Then, the position is estimated by searching the peak of a generated pseudo spectrum.

A. Constructing position-based LCX channel matrix

Define f_c as the carrier frequency, Δf as the sub-carrier spacing, $f_n = f_c + n\Delta f$ as the signal frequency at sub-carrier n . The LCX channel $\mathbf{h}[n] \in \mathbb{C}^{2 \times 1}$ for sub-carrier n is decomposed into three parts to reveal the relationship between the antenna's position and the received signal as:

$$\mathbf{h}[n] = \Xi[n] \Gamma[n] \Psi[n] \quad (5)$$

where $\Xi[n] \in \mathbb{C}^{2 \times M}$ represents the response vectors of receiving antennas:

$$\Xi[n] = \left[\xi_n^{(1)}(p), \xi_n^{(2)}(p), \dots, \xi_n^{(M)}(p) \right] \quad (6)$$

$\Gamma[n] \in \mathbb{C}^{M \times M}$ represents the LCX channel attenuation matrix:

$$\Gamma[n] = \text{diag} \left\{ \gamma_n^{(1)}(p), \gamma_n^{(2)}(p), \dots, \gamma_n^{(M)}(p) \right\} \quad (7)$$

and $\Psi[n] \in \mathbb{C}^{M \times 1}$ represents the vector of time delay:

$$\Psi[n] = \left[\psi_n^{(1)}(p, v), \psi_n^{(2)}(p, v), \dots, \psi_n^{(M)}(p, v) \right]^T \quad (8)$$

For the response vectors of receiving antennas, antenna 1 is defined as the phase center of the dual antenna. Then, we have the response vector $\xi_n^{(i)}(p) \in \mathbb{C}^{2 \times 1}$ as:

$$\xi_n^{(i)}(p) = \left[1, e^{-j \frac{2\pi c}{f_n} d_a \sin(\theta^{(i)})} \right]^T \quad (9)$$

where $\theta^{(i)}$ is azimuth angle between the antenna 1 and slot i . According to the geometric relationship in Fig.2, it satisfies:

$$\theta^{(i)} = \arctan\left(\frac{h}{p - (i-1)d}\right) \quad (10)$$

For the LCX channel attenuation matrix, it consists of two parts: wired and wireless attenuation. For the wired part, it only depends on the structure of the LCX. Then, the wired attenuation is just numerically equal to (3):

$$\left|\gamma_{wired,n}^{(i)}\right| = 10^{-\frac{\alpha_0 d(i-1)}{2000}} \quad (11)$$

The wireless part depends on the structure of the LCX and the antenna's position. According to the geometric relationship in Fig.2, The distance between the antenna and slot i is:

$$r^{(i)} = \sqrt{(p - (i-1)d)^2 + h^2} \quad (12)$$

Then, after taking (10) and (12) into $E^{(i)}$ in (1) and rearranging items, the wireless attenuation can be derived as:

$$\left|\gamma_{wireless,n}^{(i)}(p)\right| = \frac{h}{h^2 + (p - (i-1)d)^2} \quad (13)$$

Now, combining the wired part and wireless part, we have the LCX channel attenuation:

$$\gamma_n^{(i)}(p) = \left|\gamma_{wired,n}^{(i)}\right| \left|\gamma_{wireless,n}^{(i)}(p)\right| \quad (14)$$

For the vector of time delay, it represents frequency domain phase shift. The time delay depends on the signal's propagation path and the material it travels in. It consists of wired part $\tau_{wired}^{(i)} = \sqrt{\varepsilon_r}d(i-1)/c$ and wireless part $\tau_{wireless}^{(i)}(p) = \sqrt{(p - (i-1)d)^2 + h^2}/c$. Notice that there are different relative speeds between the antenna and slots. Therefore, the Doppler frequency of slot i for sub-carrier n is:

$$f_{d,n}^{(i)}(v) = \frac{vf_n}{c} \cos(\theta^{(i)}) \quad (15)$$

Combining their corresponding frequency domain phase shift, we have:

$$\psi_n^{(i)}(p, v) = e^{-j2\pi [f_n \tau_{wired}^{(i)} + (f_n + f_{d,n}^{(i)}(v)) \tau_{wireless}^{(i)}(p, v)]} \quad (16)$$

B. Position estimation through pseudo spectrum

The LCX channel matrix for all sub-carriers $\mathbf{H} \in \mathbb{C}^{N \times 2}$ is:

$$\mathbf{H} = [\mathbf{h}[0], \mathbf{h}[1], \dots, \mathbf{h}[N-1]]^T \quad (17)$$

where N is the amount of sub-carriers. When a known sequence $\mathbf{x} = [x[0], x[1], \dots, x[N-1]]^T \in \mathbb{C}^{N \times 1}$ is transmitted via LCX for each sub-carrier $n = 0, 1, \dots, N-1$, the received signal $\mathbf{y}[n] \in \mathbb{C}^{2 \times 1}$ for sub-carrier n is:

$$\mathbf{y}[n] = \mathbf{h}[n] x[n] + \mathbf{n}[n] \quad (18)$$

where $\mathbf{n} \in \mathbb{C}^{2 \times 1}$ is the additive noise vector for sub-carrier n . Our goal is now to estimate position p from the received signal for all sub-carrier $\mathbf{y} = [\mathbf{y}[0], \mathbf{y}[1], \dots, \mathbf{y}[N-1]]^T \in \mathbb{C}^{N \times 2}$.

It can be observed from Section III-A and (17) that the LCX channel matrix is only related to the receiver's position and speed under a certain LCX structure. Denote $\mathbf{h}_n(p, v)$ as

the function of $\mathbf{h}[n]$ with respect to p and v . Then, a pseudo spectrum is generated as:

$$\mathcal{P}_S(p, v) = \frac{1}{\sum_{n=0}^{N-1} \|\mathbf{y}[n] - \mathbf{h}_n(p, v) x[n]\|_2^2}, \quad p \in [0, (M-1)d], v \in [0, v_{max}] \quad (19)$$

where $\|\bullet\|_2$ denotes the process of Euclidean norm. v_{max} is the maximum speed of the train. It is obvious that the pseudo spectrum peaks around the actual position and speed:

$$(\hat{p}, \hat{v}) = \arg \max_{p, v} \mathcal{P}_S(p, v) \quad (20)$$

Notice that the signal from each slot attenuates rapidly in free space. As a result, only the closer slots have significant impacts on the received signal. For the slots that are close to receiver, their Doppler shifts are close to 0 according to (15), which do not significantly affect the pseudo spectrum. Therefore, (20) degenerates to:

$$\hat{p} \approx \arg \max_p \mathcal{P}_S(p, v=0) \quad (21)$$

The estimation position can be obtained by searching the peak of (21).

IV. A TWO-STAGE LCX POSITIONING METHOD

The error of (21) depends on the resolution of positioning signal. To further improve the positioning accuracy, signal with higher phase/time resolution and the corresponding positioning algorithm must be designed. In this section, a novel communication-positioning integration signal for LCX positioning with centimeter-level ranging capability is proposed. Then, using the novel signal waveform, a two-stage LCX positioning method based on the MSD algorithm is introduced.

A. Foundation: A novel communication-positioning integration signal for LCX positioning

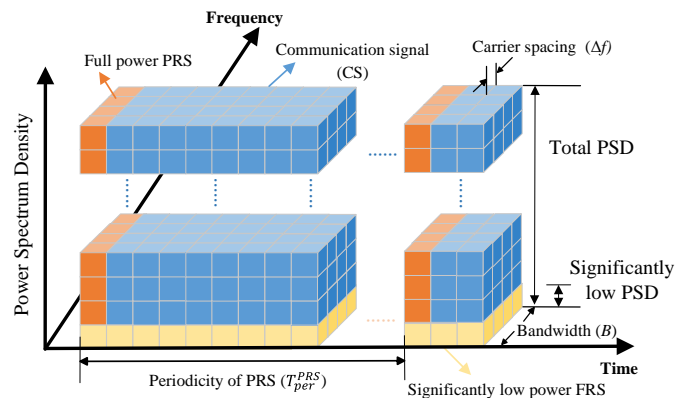


Fig. 3. Signal Structure of the novel communication-positioning integration signal for LCX positioning.

As shown in Fig.3, the proposed novel downlink communication-positioning integration signal is composed of traditional PRS and a significantly low power continuous FRS. FRS is superposed upon the existing cellular signal using

NOMA principle to mitigate its interference to communication. Both the PRS and FRS waveforms could be configured within the 5G/6G context, through 3GPP TS 38.211 [25]. Pseudorandom codes are employed for spreading gains and carrier phase integer ambiguity elimination. The specific parameters for their configurations will depend on the positioning requirements.

Define P and B as the power and bandwidth, respectively. Without loss of generality, we assume: 1) The bandwidths of PRS, FRS and CS are identical, i.e. $B_{PRS} = B_{FRS} = B_{CS} = B$; 2) The sub-carrier frequencies of PRS and FRS are identical, i.e. $\Delta f_{PRS} = \Delta f_{FRS} = \Delta f$; 3) The power of PRS and CS is identical, i.e. $P_{PRS} = P_{CS}$. In addition, to ensure the continuous transmission of FRS, the parameters for its configuration needs to satisfy:

- The size of the downlink FRS resource in the time domain $L_{FRS} = 12$;

- The combination of repetition factor and time gap $\{T_{rep}^{FRS}, T_{gap}^{FRS}\}$ is one of $\{4, 4\}$, $\{8, 8\}$, $\{16, 16\}$ and $\{32, 32\}$.

As FRS uses similar parameters to PRS, minimal adjustments are required in the higher layers such as LTE Positioning Protocol (LPP) [28] and Radio Resource Control (RRC) [29] to incorporate the communication-positioning integration signal into the 5G/6G system.

Because FRS is continuous, receiver can not only track the carrier phase for centimeter-level ranging accuracy, but also measure at any time within its calculation capacity, which is important for safety-critical applications in fast train positioning. Notice that in practical applications, some time slots are allocated to uplink communication or reserved [30]. As a result, the actual amount of time slots allocated to downlink signal is related to the practical communication configurations, which may cause discontinuous FRS transmission. However, accurate measurements are still obtainable by using intermittent signal tracking algorithms [31], [32], as long as the downlink occupies more time slots than the uplink and reserved ones.

Although FRS has the ability of high accuracy ranging and frequent measuring, traditional PRS is still necessary in our LCX positioning method for the following reasons: The tracking of FRS needs a rough position information to eliminate the signal interference between neighbor slots and fix the carrier phase integer ambiguity; The MSD algorithm hardly provides satisfactory rough position with low power FRS. Detailed explanations will be demonstrated in Section V-A.

Better than the ordinary NOMA system [33], as FRS is open to all users, it can be subtracted using Successive Interference Cancellation (SIC) after its first acquisition. Then, the interference of the FRS to PRS and CS is vanished under the assumption of perfect SIC. On the other hand, If the communication users (C-User) do not will to recover FRS for executing SIC under the consideration of power and computation consumption [34], the interference of the additive

FRS to CS will lead to BER degeneration as:

$$\Delta BER = \Gamma \left[\operatorname{erfc} \left(\frac{\gamma P_{CS}}{P_{FRS} + 2N_0 B} \right) - \operatorname{erfc} \left(\frac{\gamma P_{CS}}{2N_0 B} \right) \right] \quad (22)$$

where Γ and γ are determined by the modulation and coding schemes [35]. N_0 is the single-sided Power Spectral Density (PSD) of the environment noise. Comparing to the NOMA communication system in which the superposed CS is much stronger than FRS, there is much lower interference to the full-power CS in our proposed signal.

B. The first stage - Closest slot estimation by MSD algorithm

The first stage of LCX positioning is estimating the closest slot between the receiver and LCX. Notice that the pseudo spectrum is searched at a searching step Δp . Because there are only a limited amount of LCX slots (M slots), it's reasonable to set $\Delta p = d$. Therefore, the slot index corresponding to the peak (noted as η_l) is the closest slot estimation. Then, the rough position estimation of antenna l could also be obtained by:

$$\hat{p}_l = (\eta_l - 1) d \quad (23)$$

C. The second stage - FRS boost: centimeter-level LCX positioning algorithm

The second stage of LCX positioning is tracking the carrier phase of the continuous FRS for centimeter-level measuring. Because the FRSs from different slots are highly coupled, it will cause severe fluctuations on the received signal, leading to inaccurate carrier phase measuring. Thanks to the closest slot estimation η_l obtained from the first stage, the interference from other slots could be reduced as:

$$\hat{y}_{FRS}^{(\eta_l)} [n] = \mathbf{q}(l) \{ \mathbf{y}_{FRS} [n] - \Xi [n] \Gamma [n] \mathbf{U}(\eta_l) \Psi [n] x_{FRS} [n] \} \quad (24)$$

where $\hat{y}_{FRS}^{(\eta_l)} [n]$ is antenna l 's received FRS for sub-carrier n after interference reduction. $x_{FRS} [n]$ and $\mathbf{y}_{FRS} [n] \in \mathbb{C}^{2 \times 1}$ are the transmitted FRS symbol and the received FRS for sub-carrier n , respectively. $\mathbf{q}(l) \in \mathbb{C}^{1 \times 2}$ and $\mathbf{U}(\eta_l) \in \mathbb{C}^{M \times M}$ are defined as the antenna selection vector and the slot selection matrix, respectively. They satisfy:

$$\mathbf{q}(l) = \begin{cases} [1, 0] & l = 1 \\ [0, 1] & l = 2 \end{cases} \quad (25)$$

$$\mathbf{U}(\eta_l) = \operatorname{diag} \left\{ \underbrace{1, \dots, 1}_{1 \sim (\eta_l - 1)}, 0, \underbrace{1, \dots, 1}_{(\eta_l + 1) \sim M} \right\} \quad (26)$$

Then, antenna l 's estimated received FRS for all sub-carrier $\hat{\mathbf{y}}_{FRS}^{(\eta_l)} \in \mathbb{C}^{N \times 1}$ is expressed as:

$$\hat{\mathbf{y}}_{FRS}^{(\eta_l)} = \left[\hat{y}_{FRS}^{(\eta_l)} [0], \hat{y}_{FRS}^{(\eta_l)} [1], \dots, \hat{y}_{FRS}^{(\eta_l)} [N - 1] \right]^T \quad (27)$$

According to (24)-(27), it is clear that only the signals radiated from slot η_l are kept while the others are eliminated. Although the closest slot estimations may have errors, the kept signals are still strong enough to provide accurate phase measurements as long as the errors are not too large.

There are two types of measurement at the receiver: the carrier phase ϕ in meter measured by a Phase Locked Loop (PLL) and the code phase C in meter measured by a Delay Locked Loop (DLL) [36]. The carrier phase is measured in fractions of a wavelength, which allows for more precise positioning compared to code phase measurements. However, the receiver cannot directly determine the exact number of full cycles that have occurred. It can only measure the accumulated phase with respect to a reference point. The inability to directly determine the integer number of cycles leads to integer ambiguity k in carrier phase measurements.

Therefore, the key to high precision positioning is solving the integer ambiguity of carrier phase. In the LCX positioning scenario, because the signals radiated from different slots are used to reduce the interference from other slots, cycle slips occur frequently at each measuring. Conventional method cannot fix the integer ambiguity as it needs to be re-estimated every time when the closest slot changes. Therefore, we introduce a novel integer ambiguity estimating method by using the closest slot estimations to compensate the cycle slips and obtain the integer ambiguities in real-time.

The observation equations are built upon the relationship between the observed phase measurements and the geometric model in Fig.2. As the phase shift of the signal is not only related to the propagation path but also the material that the signal travels in, the phase shift of the wired and wireless part can be expressed as $\sqrt{\varepsilon_r}d(\eta_l-1)/\lambda$ and $\sqrt{(p-(\eta_l-1)d)^2+h^2}/\lambda$, respectively. In addition, since the system doesn't require time synchronization between the BS and the receiver, clock offset of the receiver d_{ts} can affect the phase measurements as well.

With the above elements, the observation equations of the carrier and code phases can be established as:

$$\sqrt{h^2 + (p_l - (\eta_l - 1)d)^2} + \sqrt{\varepsilon_r}d(\eta_l - 1) - k_l\lambda + d_{ts} = \phi_l \quad (28)$$

$$\sqrt{h^2 + (p_l - (\eta_l - 1)d)^2} + \sqrt{\varepsilon_r}d(\eta_l - 1) + d_{ts} = C_l \quad (29)$$

Because the PRS transmit intermittently, linear interpolation is used to predict the closest slot during the intervals of PRS. Notice that (28) and (29) are underdetermined with one antenna. Therefore, dual antenna is used to obtain more observations. Another function of dual antenna is the elimination of geometric ambiguity. As Fig.4 shows, there are two possible position solutions when positioning with only one antenna, which leads to the geometric ambiguity. However, it can be eliminated with the additional equation provided by another antenna with the geometric relation:

$$p_2 = p_1 + d_a \quad (30)$$

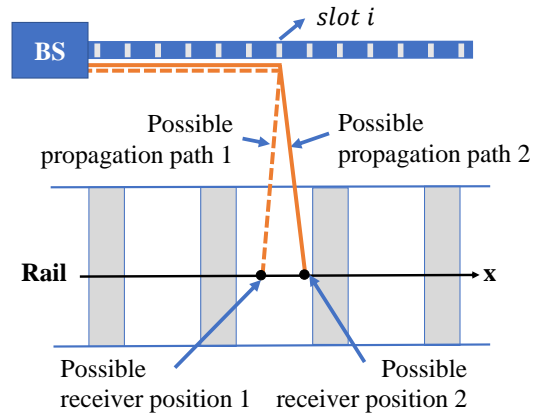


Fig. 4. The geometric ambiguity with one antenna.

Taking (30) into (28) and (29), the observation equations of all antennas can be written as (31). Note $f(p, d_{ts}, k_1, k_2) = \mathbf{z}$ as the function form of (31), where $\mathbf{z} = [C_1, C_2, \phi_1, \phi_2]^T$ is the measurement vector. Then, (31) is solved through the improved Extended Kalman Filter (EKF) where we use the slot estimation to predict the priori position. The EKF is in the form of the following set of equations:

$$\hat{\zeta}_t^- = \hat{\zeta}_{t-1} + \mathbf{u}_t \quad (32)$$

$$\mathbf{V}_t^- = \mathbf{V}_{t-1} + \mathbf{Q} \quad (33)$$

$$\mathbf{K}_t = \mathbf{V}_t^- \mathbf{G}_t^T (\mathbf{G}_t \mathbf{V}_t^- \mathbf{G}_t^T + \mathbf{R})^{-1} \quad (34)$$

$$\hat{\zeta}_t = \hat{\zeta}_t^- + \mathbf{K}_t (\mathbf{z}_t^T - \mathbf{G}_t \hat{\zeta}_t^-) \quad (35)$$

$$\mathbf{V}_t = \mathbf{I} - \mathbf{K}_t \mathbf{G}_t \quad (36)$$

where the footnote t represents time instance. Implementing (31) and the slot estimation into the filter, the elements in the improved EKF are as follows.

$\zeta_t = [p_t, d_{ts}, k_{1,t}\lambda, k_{2,t}\lambda]^T$ is the state vector at t . \mathbf{u}_t is the control vector calculated by the slot differences between t and $t-1$:

$$\mathbf{u}_t = \begin{bmatrix} [d(\eta_{1,t} - \eta_{1,t-1}) + d(\eta_{2,t} - \eta_{2,t-1})]/2 \\ 0 \\ \langle d(\eta_{1,t} - \eta_{1,t-1})/\lambda \rangle \lambda \\ \langle d(\eta_{2,t} - \eta_{2,t-1})/\lambda \rangle \lambda \end{bmatrix} \quad (37)$$

$\langle \bullet \rangle$ stands for rounding. \mathbf{Q} , \mathbf{R} and \mathbf{V}_t are the covariance of process noise, observation noise and estimate covariance at t , respectively. \mathbf{G}_t is the Jacobian matrix of $f(p_t, d_{ts}, k_{1,t}, k_{2,t})$ at t :

$$\mathbf{G}_t = \begin{bmatrix} \frac{p_t - (\eta_{1,t} - 1)d}{\sqrt{h^2 + (p_t - (\eta_{1,t} - 1)d)^2}} & 1 & 0 & 0 \\ \frac{p_t + d_a - (\eta_{2,t} - 1)d}{\sqrt{h^2 + (p_t + d_a - (\eta_{2,t} - 1)d)^2}} & 1 & 0 & 0 \\ \frac{p_t - (\eta_{1,t} - 1)d}{\sqrt{h^2 + (p_t - (\eta_{1,t} - 1)d)^2}} & 1 & -1 & 0 \\ \frac{p_t + d_a - (\eta_{2,t} - 1)d}{\sqrt{h^2 + (p_t + d_a - (\eta_{2,t} - 1)d)^2}} & 1 & 0 & -1 \end{bmatrix} \quad (38)$$

\mathbf{K}_t is the Kalman gain at t . \mathbf{I} is the identity matrix.

Having obtained the float solutions of ambiguity $\hat{k}_{1,t}$ and $\hat{k}_{2,t}$, the next step is to solve the integer ambiguity. Firstly, note

$$\left\{ \begin{array}{l} \sqrt{h^2 + (p - (\eta_1 - 1)d)^2} + \sqrt{\varepsilon_r}d(\eta_1 - 1) + d_{ts} = C_1 \\ \sqrt{h^2 + (p + d_a - (\eta_2 - 1)d)^2} + \sqrt{\varepsilon_r}d(\eta_2 - 1) + d_{ts} = C_2 \\ \sqrt{h^2 + (p - (\eta_1 - 1)d)^2} + \sqrt{\varepsilon_r}d(\eta_1 - 1) - k_1\lambda + d_{ts} = \phi_1 \\ \sqrt{h^2 + (p + d_a - (\eta_2 - 1)d)^2} + \sqrt{\varepsilon_r}d(\eta_2 - 1) - k_2\lambda + d_{ts} = \phi_2 \end{array} \right. \quad (31)$$

$\hat{\mathbf{a}}_t = [\hat{p}_t, \hat{d}_{ts}]^T$ and $\hat{\mathbf{b}}_t = [\hat{k}_{1,t}, \hat{k}_{2,t}]^T$ as the non-integer and integer state elements, respectively. Then, we have:

$$\hat{\zeta}_t = [\hat{\mathbf{a}}_t, \hat{\mathbf{b}}_t]^T \quad (39)$$

$$\begin{aligned} \mathbf{V}_t &= \begin{bmatrix} Cov(\hat{\mathbf{a}}_t, \hat{\mathbf{a}}_t) & Cov(\hat{\mathbf{a}}_t, \hat{\mathbf{b}}_t) \\ Cov(\hat{\mathbf{b}}_t, \hat{\mathbf{a}}_t) & Cov(\hat{\mathbf{b}}_t, \hat{\mathbf{b}}_t) \end{bmatrix} \\ &= \begin{bmatrix} \mathbf{S}_{\hat{\mathbf{a}}_t} & \mathbf{S}_{\hat{\mathbf{a}}_t \hat{\mathbf{b}}_t} \\ \mathbf{S}_{\hat{\mathbf{b}}_t \hat{\mathbf{a}}_t} & \mathbf{S}_{\hat{\mathbf{b}}_t} \end{bmatrix} \end{aligned} \quad (40)$$

And the integer ambiguities can be solved with:

$$\check{\mathbf{b}}_t = \min_{\mathbf{b}_t} (\hat{\mathbf{b}}_t - \mathbf{b}_t)^T \mathbf{S}_{\hat{\mathbf{b}}_t}^{-1} (\hat{\mathbf{b}}_t - \mathbf{b}_t), \mathbf{b}_t \in \mathbb{Z} \quad (41)$$

An elliptical-shaped search space is constructed to solve (41). Its shape and size are determined by the covariance $\mathbf{Q}_{\hat{\mathbf{b}}_t}$ and a constant χ^2 as:

$$(\hat{\mathbf{b}}_t - \mathbf{b}_t)^T \mathbf{S}_{\hat{\mathbf{b}}_t}^{-1} (\hat{\mathbf{b}}_t - \mathbf{b}_t) \leq \chi^2 \quad (42)$$

The shape of the elliptical search space is very thin due to the strong correlation between the float ambiguity solutions caused by the close proximity of the two antennas, which may lead to searching failure [16]. Integer Gauss transformation is employed to decorrelate the ambiguities. Denote the transformation matrix as \mathbf{W} . Then, \mathbf{b}_t , $\hat{\mathbf{b}}_t$ and $\mathbf{Q}_{\hat{\mathbf{b}}_t}$ are transformed as:

$$\mathbf{w}_t = \mathbf{W}\mathbf{b}_t \quad (43)$$

$$\hat{\mathbf{w}}_t = \mathbf{W}\hat{\mathbf{b}}_t \quad (44)$$

$$\mathbf{S}_{\mathbf{w}} = \mathbf{W}\mathbf{S}_{\hat{\mathbf{b}}_t}\mathbf{W} \quad (45)$$

Taking (43)-(45) into (41) and (42), we have:

$$\check{\mathbf{w}}_t = \min_{\mathbf{z}_t} (\hat{\mathbf{w}}_t - \mathbf{z}_t)^T \mathbf{S}_{\mathbf{w}}^{-1} (\hat{\mathbf{w}}_t - \mathbf{z}_t) \quad (46)$$

$$(\hat{\mathbf{w}}_t - \mathbf{z}_t)^T \mathbf{S}_{\mathbf{w}}^{-1} (\hat{\mathbf{w}}_t - \mathbf{z}_t) \leq \chi^2 \quad (47)$$

Next is to determine the size of the search space (i.e. the value of χ^2). The search range can be narrowed down by theoretically calculating the possible value of the integer ambiguities with the slot estimation. According to Fig.2, when

antenna l is near slot η_l , the ambiguity of the received signal should be in the range of:

$$\begin{aligned} k &\subseteq \langle \langle (\sqrt{\varepsilon_r}d(\eta_l - 1) + h) / \lambda \rangle \rangle, \\ &\left\langle \left\langle \left(\sqrt{\varepsilon_r}d(\eta_l - 1) + \sqrt{h^2 + \left(\xi \frac{d}{2}\right)^2} \right) / \lambda \right\rangle \right\rangle \end{aligned} \quad (48)$$

where $\xi \in \mathbb{Z}^+$ is a range coefficient whose value is determined by the closest slot estimation accuracy. The more accurate closest slot estimation is, the smaller ξ should be to exclude more unnecessary integer ambiguity candidates. To calculate χ^2 , we can use the midpoint of the possible ranges by substituting χ^2 into (47):

$$\mathbf{k}_{upper} = \left\langle \left\langle \left(\sqrt{\varepsilon_r}d \left(\begin{bmatrix} \eta_{1,t} \\ \eta_{2,t} \end{bmatrix} - 1 \right) + \sqrt{h^2 + \left(\xi \frac{d}{2}\right)^2} \right) / \lambda \right\rangle \right\rangle \quad (49)$$

$$\mathbf{k}_{lower} = \left\langle \left\langle \left(\sqrt{\varepsilon_r}d \left(\begin{bmatrix} \eta_{1,t} \\ \eta_{2,t} \end{bmatrix} - 1 \right) + h \right) / \lambda \right\rangle \right\rangle \quad (50)$$

$$\mathbf{k}_{mid} = (\mathbf{k}_{upper} + \mathbf{k}_{lower}) / 2 \quad (51)$$

$$\chi^2 = (\hat{\mathbf{w}}_t - \mathbf{W}\mathbf{k}_{mid})^T \mathbf{S}_{\mathbf{w}}^{-1} (\hat{\mathbf{w}}_t - \mathbf{W}\mathbf{k}_{mid}) \quad (52)$$

Now, the transformed integer ambiguity $\check{\mathbf{w}}_t$ can be solved by searching in the search space of (47). Then, applying inverse transformation $\check{\mathbf{b}}_t = \mathbf{W}^{-1}\check{\mathbf{w}}_t$, the integer ambiguity for carrier phase is obtained and the estimation accuracy of non-integer state elements can be further improved with the solved integer ambiguity:

$$\check{\mathbf{a}}_t = \hat{\mathbf{a}}_t - \mathbf{S}_{\hat{\mathbf{a}}_t \hat{\mathbf{b}}_t} \mathbf{S}_{\hat{\mathbf{b}}_t}^{-1} (\hat{\mathbf{b}}_t - \check{\mathbf{b}}_t) \quad (53)$$

$$\mathbf{S}_{\check{\mathbf{a}}_t} = \mathbf{S}_{\hat{\mathbf{a}}_t} - \mathbf{S}_{\hat{\mathbf{a}}_t \hat{\mathbf{b}}_t} \mathbf{S}_{\hat{\mathbf{b}}_t}^{-1} \mathbf{S}_{\hat{\mathbf{b}}_t \hat{\mathbf{a}}_t} \quad (54)$$

Elements in $\check{\mathbf{a}}_t$ and $\mathbf{S}_{\check{\mathbf{a}}_t}$ are then updated back into $\hat{\zeta}_t$ and \mathbf{V}_t for future EKF instances. In order to avoid searching failure due to the inaccurate float ambiguity solution at the beginning of the filtering iteration, the integer ambiguity should only be solved after a few iterations.

The proposed two-stage LCX positioning method is summarized in Fig.5.

V. PERFORMANCE EVALUATION

In this section, we present simulation results to show the performance of the proposed MSD algorithm, the proposed two-stage LCX positioning method and the interference of the FRS to communication signal in order. We set up the

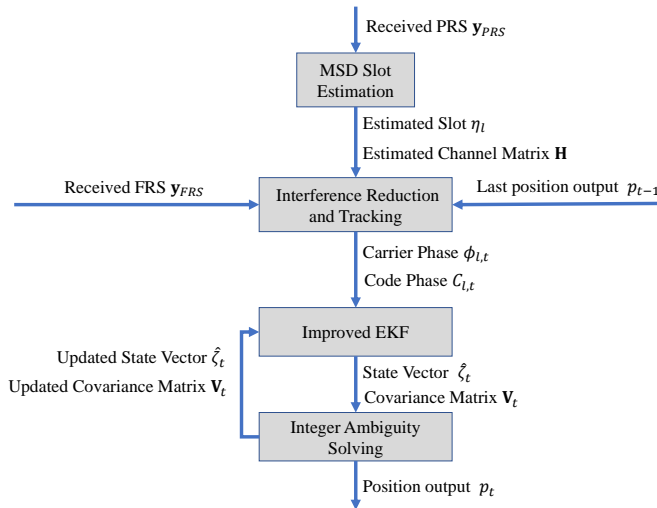


Fig. 5. Flow graph of the proposed two-stage LCX positioning method.

simulation parameters as in Table I. Railway tunnel is emulated using the Clustered Delay Line (CDL) model for LCX channel based on [37] and [38]. For each scenario, simulation is conducted with Monte Carlo method for 100 runs. Define $SNR = \frac{P_{CS}}{N_0B}$ as the communication-signal-to-noise-ratio, $FCR = \frac{P_{FRS}}{P_{CS}}$ as the communication-to-FRS-ratio and $EFNR = \frac{P_{FRS}}{P_{CS} + N_0B} = \frac{FCR}{1 + SNR^{-1}}$ as the equivalent FRS-to-noise-ratio for later use. The MUSIC-based positioning method is used as the benchmark for the performance analysis. The detail of its implementation can be seen in Appendix.A.

TABLE I
SIMULATION SETUP

Train speed v	60km/h
Relative permittivity of LCX ϵ_r [39]	1.26
Transmission attenuation of LCX α_0 [39]	9dB/100m
Distance between LCX and the rail h	1m
Carrier frequency f_c	3500MHz
Sub-carrier spacing Δf	30kHz
PRS Comb size K_{comb}^{PRS}	4
Number of consecutive OFDM symbols of PRS L_{PRS}	4
PRS resource set slot periodicity T_{per}^{PRS}	640
PRS resource repetition factor T_{rep}^{PRS}	1
The time gap of PRS T_{gap}^{PRS}	1
FRS Comb size K_{comb}^{FRS}	2
Number of consecutive OFDM symbols of FRS L_{FRS}	12
FRS resource set slot periodicity T_{per}^{FRS}	16
FRS resource repetition factor T_{rep}^{FRS}	16
The time gap of FRS T_{gap}^{FRS}	1

Without loss of generality, we use the bandwidth of 10MHz, 25MHz and 50MHz as representatives to evaluate the impact of bandwidth on our proposed algorithms in the following subsections. Using the sub-carrier spacing of $\Delta f = 30$ kHz, the corresponding relationships between bandwidth and the number of Physical Resource Blocks (PRBs) allocated for positioning are as follows: 10MHz corresponds to 24 PRBs, 25MHz corresponds to 65 PRBs, 50MHz corresponds to 133 PRBs [40].

A. Performance of MSD algorithm

Fig.6 shows the comparison between the MSD and the MUSIC-based positioning method with different bandwidths when $d = 4$ cm. It's clear that the proposed MSD algorithm has higher positioning accuracy than the MUSIC-based method with the same bandwidth. It also shows that the performance of the MSD algorithm improves as bandwidth increases. This is because with larger bandwidth, more available frequency points are calculated in (19), which results in higher time resolution. In addition, it can be observed that the performance of the MSD algorithm becomes saturate when SNR becomes larger as the dominate factor becomes the signal resolution rather than the noise. Therefore, the MSD algorithm can provide consistent positioning performance in relative high SNR.

Moreover, it shows that the performance degrades significantly in severe SNR. This is because as SNR decreases, shown in Fig.7, the peak may drift or appear in other places, resulting in large errors. Therefore, PRS is necessary in the proposed communication-positioning integration signal as the low power FRS is not suitable in MSD algorithm to obtain the satisfactory rough position which is essential to the slot interference reduction and integer ambiguity elimination. Particularly, PRS can be used in the accuracy insensitive or energy sensitive applications, like passenger guiding, because the computation of MSD algorithm is much lower than carrier phase tracking.

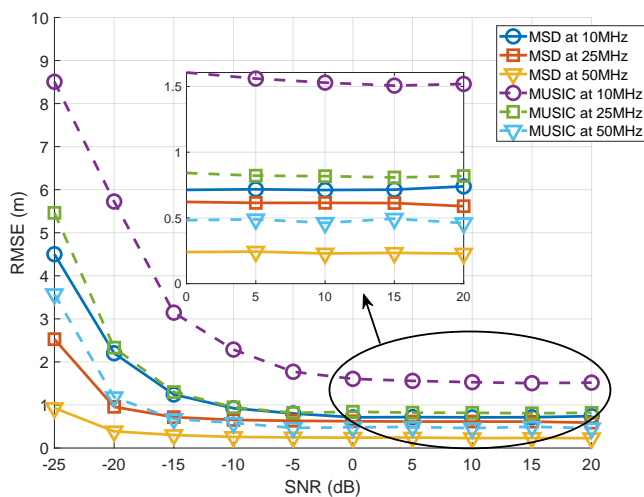
Fig.8 shows the comparison between the MSD algorithm with different LCX slot spacing when $B = 25$ MHz. It's obvious that the LCX slot spacing doesn't significantly affect performance of the MSD algorithm. This is because the effect of the LCX slot spacing on pseudo spectrum has already been identified as (19) shows. Therefore, the proposed MSD algorithm can work regardless of the LCX structure.

B. Performance of the proposed two-stage LCX positioning

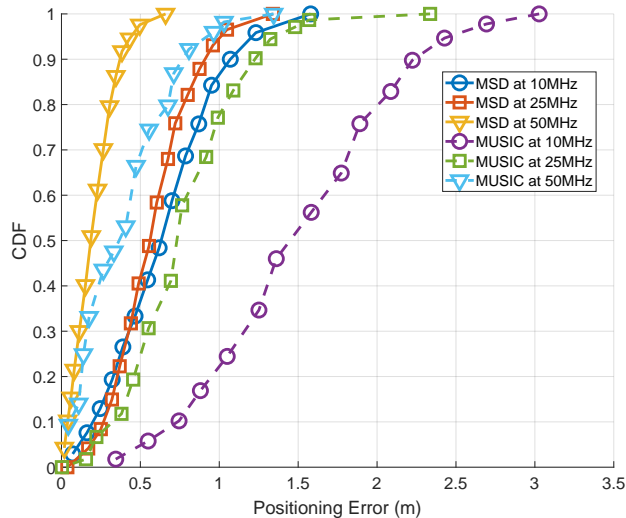
In the first stage, the closest slot is estimated. Define slot deviation as:

$$\Delta\eta = |\eta_c - \eta_e| \quad (55)$$

where η_c and η_e are the index of the actual and estimated closest slot, respectively. The average slot deviation of all Monte Carlo runs is calculated to evaluate the performance of closest slot estimation. Fig.9 shows the average slot deviation by the proposed MSD algorithm with different bandwidths and LCX slot spacing when $SNR = 0$ dB. It's obvious that the slot estimation is more accurate with larger bandwidth because the positioning accuracy is higher. However, notice that the accuracy of the closest slot estimation decreases as LCX slot spacing gets smaller. This is because with smaller slot spacing, there are more slot candidates to choose from. Although the positioning accuracy of MSD with different LCX slot spacing is similar, it's less likely to find the actual index of the closest slot. It's also shown that although the closest slot estimation may not be perfectly accurate, the deviation is small, which will not significantly impact its ability to remove the interference between slots for FRS positioning.



(a) The Root Mean Square Error (RMSE) under different SNRs.



(b) The Cumulative Distribution Functions (CDF) of positioning error ($SNR = 0\text{dB}$).

Fig. 6. The comparison between the MSD algorithm and the MUSIC-based positioning method with different bandwidths ($d = 4\text{cm}$).

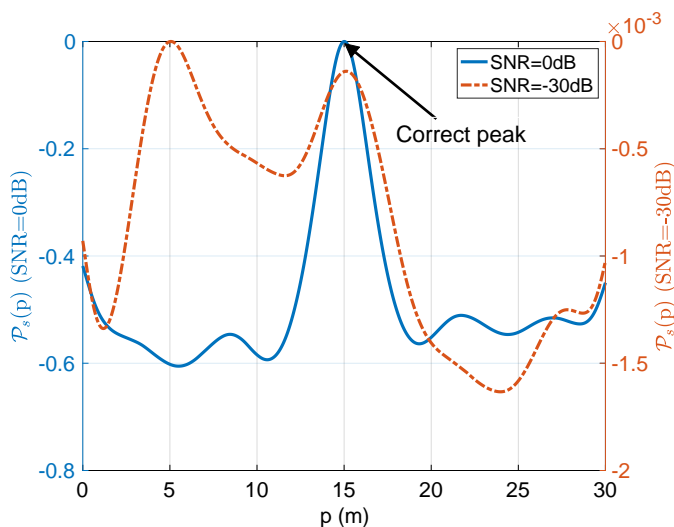


Fig. 7. The normalized pseudo spectrum with different bandwidths under different SNRs. The y-axis on left and right are the y-axis of $SNR = 0\text{dB}$ and $SNR = -30\text{dB}$, respectively.

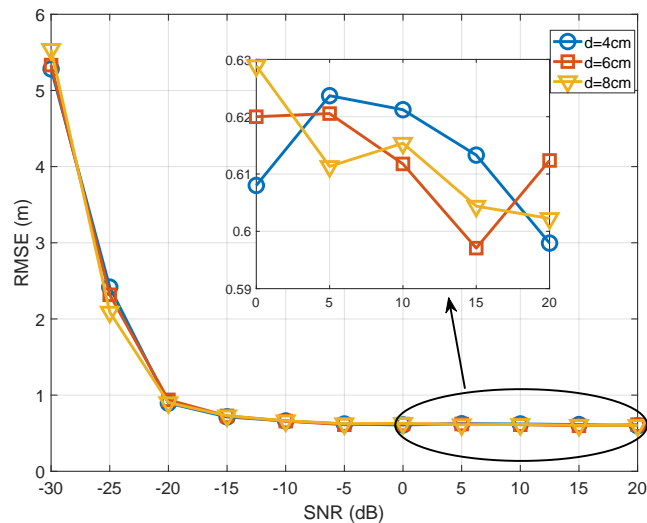


Fig. 8. Comparison between the MSD algorithm with different slot spacing ($B = 25\text{MHz}$).

In the second stage, FRS is used to obtain higher positioning accuracy. Fig.10a shows the RMSE of the proposed two-stage LCX positioning method under different communication SNRs and FCRs when $B = 25\text{MHz}$ and $d = 4\text{cm}$. It is clear that the RMSEs are at centimeter-level and increase when SNR and FCR increase because either of them leads to higher EFNR as Fig.10b shows.

Fig.11 shows the positioning accuracy of the proposed two-stage LCX positioning method with different bandwidths and slot spacing when $SNR = 0\text{dB}$ and $FCR = -25\text{dB}$. It can be observed that smaller LCX slot spacing leads to better positioning performance. This is because the positioning performance is affected by the geometric structure of

the system. As (31) is established based on the geometric relationship that is related to slot spacing, the amplification of measuring error from the smaller LCX slot spacing is smaller than the larger ones. Detailed deduction can be seen in Appendix.B. In addition, it can be seen that the positioning accuracy of our proposed method improves as the bandwidth gets larger. It is unsurprising because higher bandwidth results in more accurate slot estimation and more accurate phase measurement. Notice that the performance improvements of larger bandwidths are relatively small especially when slot spacing is small. This is also due to the smaller measuring error amplification from smaller LCX slot spacing as (71) shows. Since the carrier phase measurements are already very

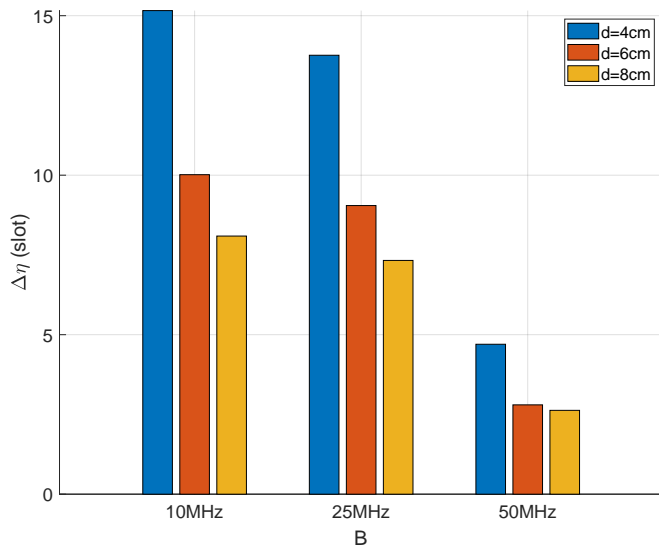


Fig. 9. The performance of closest slot estimation with different bandwidths and slot spacing ($SNR = 0\text{dB}$).

accurate, its improvement isn't going to greatly affect the performance of positioning.

C. Interference of the FRS to communication signal

Fig.12 evaluates the interference of the FRS to communication signal with BER. It is clear that the curves with different FCRs are very close to the one where $FCR = -\infty\text{dB}$ (i.e. no FRS), which means the FRS causes little interference to communication signal. In addition, as mention earlier, the C-user can remove the interference of FRS using SIC if needed. Then, the BER degeneration caused by FRS will be vanished.

VI. EXPLORING THE SYSTEM'S POTENTIAL: POSITIONING WITH REDUNDANT INFRASTRUCTURE

In certain scenarios, multiple LCXs may also be deployed for improved communication reliability and coverage within the tunnel environments. To explore the potential of the proposed system, building upon the original focus of high precision train positioning with one LCX, we expand our research to see how our proposed methodology performs with redundant infrastructure. Specifically, in this section, we investigate how an additional LCX affects the system's positioning accuracy, robustness, and explore its possible extension to 2D positioning. We will describe how our system can be extended in detail, present the corresponding simulation results and analyze their possible applications.

A. Improvement in positioning accuracy and robustness

As Fig.13 shows, an additional parallel LCX is placed on the other side of the tunnel to provide an additional signal channel to the receiver. Denote $s = 1, 2$ as the index of the LCX. $\eta_l^{(s)}$ is the estimated index of the closest slot between antenna l and LCX s . $h^{(s)}$ is the vertical distance between LCX s and the antenna. Without loss of generality, assume

the two LCXs are the same (with the same slot spacing d and permittivity $\sqrt{\epsilon_r}$) and define the projection of LCX 1's first slot on the rail track as the origin.

To extend the original algorithm into 2 LCXs, 4 additional equations that are related to the other LCX will be added into (31). The equation set can be rewritten as (56), where $d_{t,s}^{(s)}$ is the clock offset between the receiver and LCX s and $k_l^{(s)}$ is the carrier phase ambiguity of the signal from LCX s received by antenna l . Notice that (56) contains 8 equations (4 equations for $s = 1$ and another 4 for $s = 2$) and the equations for each LCX are established independently with the measurements from each signal channel.

When the signals from both LCXs are available, the position of the train can be obtained by solving (56) through the EKF methodology described in Section IV-C. The details of (33) to (52) will need to be adjusted accordingly to solve the additional equations in (56). The detailed adjustments for EKF are listed in Appendix.C.

Fig.14 shows the positioning performance of the dual-LCX setup. It's unsurprising to see that the redundant observations provided by the other LCX can improve the overall positioning accuracy of the system. Specifically, the additional LCX is able to improve the RMSE by 14.5%. In scenarios that require precise monitoring and control, such accuracy improvement is significant.

In addition to improving accuracy, the dual-LCX setup can also improve the robustness of the system. For example, when considering train operations, it is common to observe scenarios where two trains pass each other. These instances are a regular occurrence and necessitate careful coordination to ensure smooth and efficient operations. If there is only one LCX, the positioning accuracy of the opposite train may be compromised because the train closer to the LCX could block the signal.

The dual-LCX system is able to handle such scenario. Although the dual-LCX system in Fig.13 only contains one rail track, it can be applied to scenarios with multiple rail tracks as well. Each train can utilize the proposed methodology for positioning, with the only difference being the change in the coordinate system. When there is only one train in presence, the positioning accuracy is improved by the additional LCX. When the other train blocks the signal, the system is still able to obtain centimeter-level positioning accuracy positioning result by solving (31) through the measurements from the unblocked LCX, which ensures the positioning system to remain robust and reliable.

Notice that alternative methods such as vehicle-mounted Inertial Navigation Systems (INS) can be employed to ensure the safety of the train through multi source fusion as well [41], [42], but they are out of the scope of this paper.

B. Extension to 2D positioning

The additional LCX also enables the system's ability to conduct high-accuracy 2D positioning by providing additional measurements. In Fig.13, the x-axis represents the direction along the rail track, while the y-axis represents the vertical

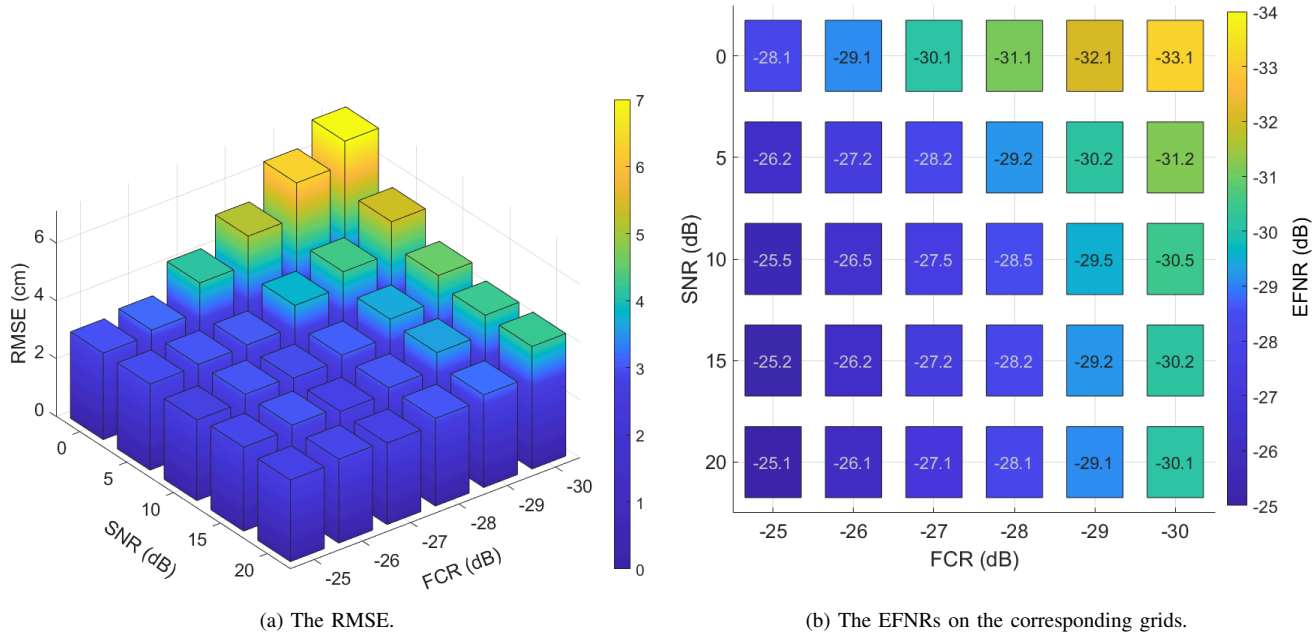


Fig. 10. The proposed two-stage LCX positioning accuracy with different SNRs and FCRs ($B = 25\text{MHz}$, $d = 4\text{cm}$).

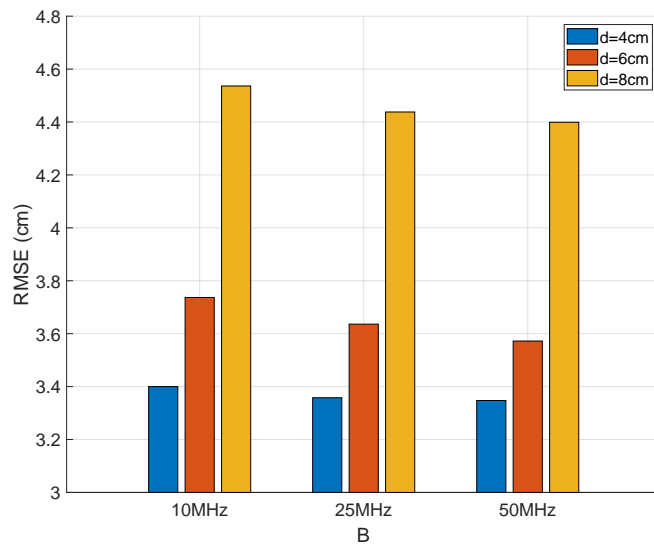


Fig. 11. The proposed two-stage LCX positioning accuracy using FRS with different bandwidths and slot spacing ($SNR = 0\text{dB}$ and $FCR = -25\text{dB}$).

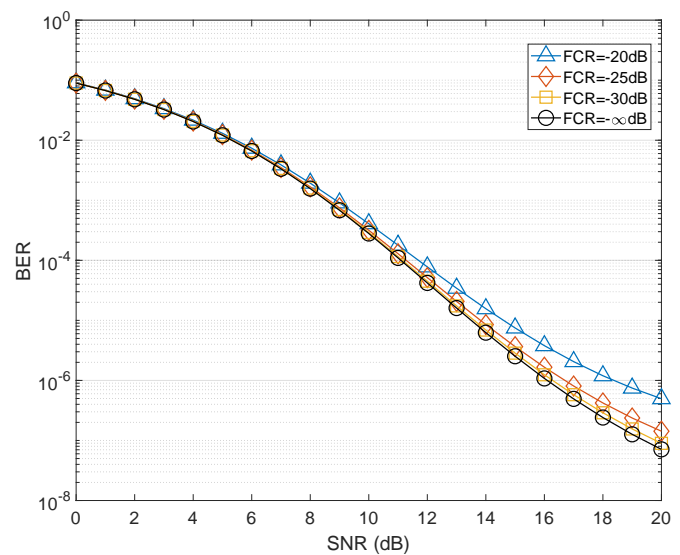


Fig. 12. The BER with different FCRs under different SNRs in tunnel scenario.

direction relative to the rail track. Different from Section VI-A, the vertical distance between LCX s and the antenna needs to be calculated with the y coordinates of the receiver and the LCX. Denote (p_x, p_y) as the coordinate of the receiver and $p_{LCX}^{(s)}$ as the y coordinate of LCX s . Then, (56) can be adjusted to (57) for 2D positioning.

The receiver position (p_x, p_y) can be solved through the improved EKF. The details of the adjustments in EKF for 2D positioning are listed in Appendix.D.

Fig.15 shows the performance of 2D LCX positioning. It can be seen that the system still provides high accuracy

positioning performance after being expanded into 2D. Notice that the accuracy in y direction is higher than x direction. It's because the measuring error will result more positioning error in x direction rather than y direction, which is shown in Fig.16. It's also unsurprising to see that the accuracy of 1-Dimensional (1D) positioning is higher than 2D positioning. This is because for 1D positioning, the error in y direction is eliminated by the prior knowledge of rail track information during the calculation.

As trains move along their rail tracks and the trajectories of these tracks are generally known, 1D positioning to locate

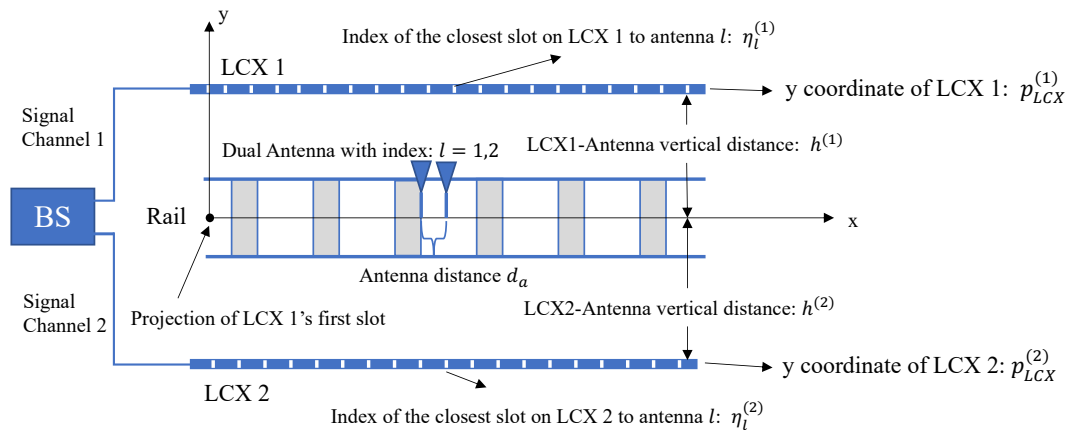


Fig. 13. The geometric relationship of the dual-LCX system.

$$\left\{ \begin{array}{l} \sqrt{(h^{(s)})^2 + (p - (\eta_1^{(s)} - 1)d)^2} + \sqrt{\varepsilon_r}d(\eta_1^{(s)} - 1) + d_{ts}^{(s)} = C_1^{(s)} \\ \sqrt{(h^{(s)})^2 + (p + d_a - (\eta_2^{(s)} - 1)d)^2} + \sqrt{\varepsilon_r}d(\eta_2^{(s)} - 1) + d_{ts}^{(s)} = C_2^{(s)} \\ \sqrt{(h^{(s)})^2 + (p - (\eta_1^{(s)} - 1)d)^2} + \sqrt{\varepsilon_r}d(\eta_1^{(s)} - 1) - k_1^{(s)}\lambda + d_{ts}^{(s)} = \phi_1^{(s)} \\ \sqrt{(h^{(s)})^2 + (p + d_a - (\eta_2^{(s)} - 1)d)^2} + \sqrt{\varepsilon_r}d(\eta_2^{(s)} - 1) - k_2^{(s)}\lambda + d_{ts}^{(s)} = \phi_2^{(s)} \end{array} \right. \quad (56)$$

$$\left\{ \begin{array}{l} \sqrt{(p_y - p_{LCX}^{(s)})^2 + (p_x - (\eta_1^{(s)} - 1)d)^2} + \sqrt{\varepsilon_r}d(\eta_1^{(s)} - 1) + d_{ts}^{(s)} = C_1^{(s)} \\ \sqrt{(p_y - p_{LCX}^{(s)})^2 + (p_x + d_a - (\eta_2^{(s)} - 1)d)^2} + \sqrt{\varepsilon_r}d(\eta_2^{(s)} - 1) + d_{ts}^{(s)} = C_2^{(s)} \\ \sqrt{(p_y - p_{LCX}^{(s)})^2 + (p_x - (\eta_1^{(s)} - 1)d)^2} + \sqrt{\varepsilon_r}d(\eta_1^{(s)} - 1) - k_1^{(s)}\lambda + d_{ts}^{(s)} = \phi_1^{(s)} \\ \sqrt{(p_y - p_{LCX}^{(s)})^2 + (p_x + d_a - (\eta_2^{(s)} - 1)d)^2} + \sqrt{\varepsilon_r}d(\eta_2^{(s)} - 1) - k_2^{(s)}\lambda + d_{ts}^{(s)} = \phi_2^{(s)} \end{array} \right. \quad (57)$$

the train's position on the track is sufficient. However, in cases such as junctions or accident monitoring where the exact track information is unavailable, the 2D positioning ability becomes necessary to determine the train's location accurately.

2D positioning also offers valuable implications on car scenarios such as 5G/6G-based Connected Automated Vehicles (CAV) as well. Such scenario introduces complexities related to lane-specific positioning and tracking. Therefore, precise 2D positioning becomes crucial for effectively managing traffic flow and ensuring optimal safety measures. When the 2D positioning methodology is applied in cars, x-axis will represent the direction along the lane, and the y-axis will represent the vertical direction relative to the lane. Simulation shows that the 2D LCX positioning accuracy in the y direction is sufficient to differentiate the lanes that the car is driving on. Although tunnels for cars are now commonly equipped with conventional antennas for communication and positioning, because the methodology in this paper has significant advantage in 2D

positioning accuracy, it is compelling to deploy multiple LCXs for such scenario in the future.

VII. CONCLUSION

In this paper, we presented a feasibility study for a centimeter-level train positioning methodology using LCX as antenna for the upcoming B5G/6G rail use cases in intelligent transportation systems. A low-complexity Multiple Slot Distinction (MSD) LCX positioning algorithm is proposed to obtain a decimeter-level accuracy. Simulation results show that our proposed MSD algorithm outperforms the traditional MUSIC-based LCX positioning methods. To further improve the positioning accuracy to centimeter-level and increase the measuring frequency for fast train, a novel communication-positioning integration signal is designed. This signal superposes a significantly low power Fine Ranging Signal (FRS) to the traditional cellular signal using Non-Orthogonal Multiple Access (NOMA) principle for a continuous transmission.

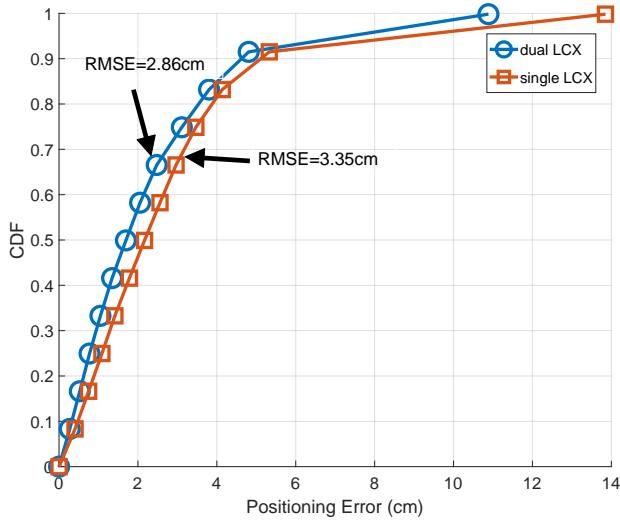


Fig. 14. The cumulative distribution functions (CDF) of positioning error of the expanded dual-LCX positioning method ($B = 25\text{MHz}$, $d = 4\text{cm}$, $\text{SNR} = 0\text{dB}$ and $\text{FCR} = -25\text{dB}$).

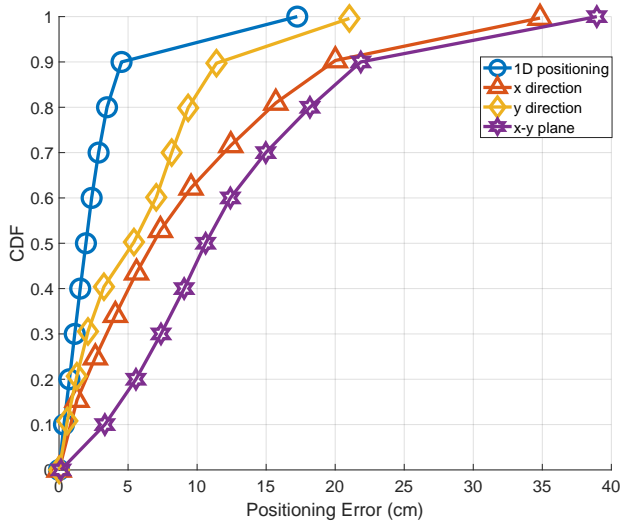


Fig. 15. The cumulative distribution functions (CDF) of positioning error of the expanded 2D two-stage LCX positioning method ($B = 25\text{MHz}$, $d = 4\text{cm}$, $\text{SNR} = 0\text{dB}$ and $\text{FCR} = -25\text{dB}$).

Then, the full-power Positioning Reference Signal (PRS) in traditional cellular signal along with the proposed FRS works together to realize a two-stage positioning: At the first stage, the closest slot between the receiver and LCX is estimated by the proposed MSD algorithm using PRS; At the second stage, carrier phase of the continuous FRS is tracked for centimeter-level positioning, using the new slot interference reduction and integer ambiguities elimination algorithms with the help of the closest slot estimation. The numerical results show our proposed two-stage LCX positioning method along with the novel PRS+FRS waveform improves the positioning accuracy dramatically than traditional methods. And FRS causes a negligible Bit Error Rate (BER) loss which means FRS has little interference to Communication Signal (CS). Lastly, the method's positioning potential with redundant infrastructure

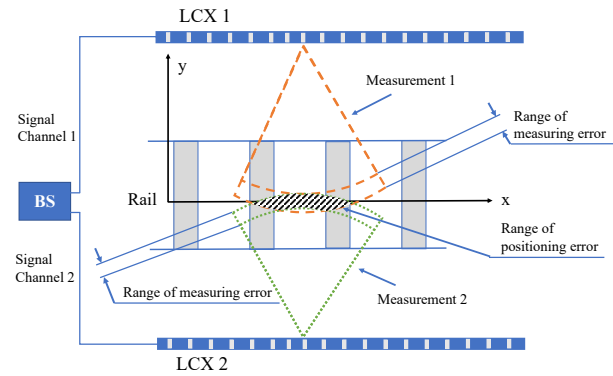


Fig. 16. The relationship between measuring error and positioning error.

is explored. Analysis and simulations shows that the redundant infrastructure can improve the positioning accuracy and robustness of the system, while enabling its 2-Dimensional (2D) positioning ability.

APPENDIX

A. The implementation of the MUSIC-based positioning method

The MUSIC-based positioning method considers the signal from the closest slot as the primary source, while regarding the signals from other slots as multipath components. It utilizes the TOA estimation MUSIC algorithm to estimate the time delay and solve the position based on geometric relationships. The relationship between one antenna's received signal $\mathbf{y}_{\mathcal{M}} \in \mathbb{C}^{N \times 1}$ and the transmitted signal $\mathbf{x} \in \mathbb{C}^{N \times 1}$ can be expressed by:

$$\mathbf{y}_{\mathcal{M}} = \sum_{m_s=1}^{M_s} |\alpha_{\mathcal{M},m_s}| \mathbf{a}_{\mathcal{M}}(\tau_{\mathcal{M},m_s}) \odot \mathbf{x} + \mathbf{n} \quad (58)$$

where \odot represents the process of Hadamard product. M_s is the amount of sources. $\alpha_{\mathcal{M},m_s}$ is the complex attenuation of the signal from source m_s . $\mathbf{n} \in \mathbb{C}^{N \times 1}$ is the additive noise vector. $\mathbf{a}_{\mathcal{M}}(\tau_{\mathcal{M},m_s}) \in \mathbb{C}^{N \times 1}$ is a column vector composed of Fourier operators that are related to the time delay of the signal from source m_s , which is expressed as:

$$\mathbf{a}_{\mathcal{M}}(\tau_{\mathcal{M},m_s}) = [e^{-j2\pi f_0 \tau_{\mathcal{M},m_s}}, \dots, e^{-j2\pi f_{N-1} \tau_{\mathcal{M},m_s}}]^T \quad (59)$$

To estimate the time delay with the received signal $\mathbf{y}_{\mathcal{M}}$, the correlation matrix of $\mathbf{y}_{\mathcal{M}}$ is required, which is expressed by:

$$\mathbf{R}_{\mathcal{M}} = \mathbb{E} \{ \mathbf{y}_{\mathcal{M}} \mathbf{y}_{\mathcal{M}}^H \} \quad (60)$$

where $\mathbb{E} \{ \bullet \}$ represents the ensemble average, and H represents the Hermitian transpose. Define $\mathbf{R}_{\mathbf{y}\mathbf{y}}$'s eigenvalues and eigenvectors as $\varrho_1, \varrho_2, \dots, \varrho_N$ ($\varrho_1 \geq \dots \geq \varrho_N$) and $\varsigma_1, \varsigma_2, \dots, \varsigma_N$, respectively. The eigenvectors of $\mathbf{R}_{\mathbf{y}\mathbf{y}}$ can be divided into signal space $\mathbf{E}_{\mathbf{S}} = [\varsigma_1, \varsigma_2, \dots, \varsigma_M] \in \mathbb{C}^{N \times M}$ and noise space $\mathbf{E}_{\mathbf{N}} = [\varsigma_{M+1}, \varsigma_{M+2}, \dots, \varsigma_N] \in \mathbb{C}^{N \times (N-M)}$. Then, the pseudo spectrum $\mathcal{P}_{\mathcal{S}}(\tau_{\mathcal{M}})$ is generated using the noise space $\mathbf{E}_{\mathbf{N}}$ and the Fourier operator with different $\tau_{\mathcal{M}}$:

$$\mathcal{P}_{\mathcal{M}}(\tau_{\mathcal{M}}) = \frac{\mathbf{a}_{\mathcal{M}}^H(\tau_{\mathcal{M}}) \mathbf{a}_{\mathcal{M}}(\tau_{\mathcal{M}})}{\mathbf{a}_{\mathcal{M}}^H(\tau_{\mathcal{M}}) \mathbf{E}_{\mathbf{N}} \mathbf{E}_{\mathbf{N}}^H \mathbf{a}_{\mathcal{M}}(\tau_{\mathcal{M}})} \quad (61)$$

And the peak of $\mathcal{P}_{\mathcal{M}}(\tau_{\mathcal{M}})$ is the desired time delay:

$$\hat{\tau}_{\mathcal{M}} = \arg \max_{\tau_{\mathcal{M}}} \mathcal{P}_{\mathcal{M}}(\tau_{\mathcal{M}}) \quad (62)$$

Then, based on the geometry of the system model in Fig.2, the TOA of the received signal is:

$$\hat{\tau}_{\mathcal{M}} = \frac{1}{c} (\varepsilon_r p + h) \quad (63)$$

And the position can be obtained with:

$$p = \frac{1}{\varepsilon_r} (c\hat{\tau}_{\mathcal{M}} - h) \quad (64)$$

For dual antenna, the position can be obtained by solving:

$$\begin{cases} \hat{\tau}_{\mathcal{M}}^{(1)} = \frac{1}{c} (\varepsilon_r p + h) \\ \hat{\tau}_{\mathcal{M}}^{(2)} = \frac{1}{c} (\varepsilon_r (p + d_a) + h) \end{cases} \quad (65)$$

where $\hat{\tau}_{\mathcal{M}}^{(l)}$ is the TOA estimation of antenna l .

B. The amplification of measuring error with different LCX slot spacing

Based on (28), the relationship between p_l and ϕ_l can be expressed as function $g(\phi_l)$:

$$p_l = g(\phi_l) = (\eta_l - 1)d \pm \sqrt{(\phi_l + k_l\lambda - \sqrt{\varepsilon_r}d(\eta_l - 1) - d_{ts})^2 + h^2} \quad (66)$$

Defining the carrier phase measuring error as $\Delta\phi_l$, the relationship between the measured carrier phase $\check{\phi}_l$ and the actual one ϕ_l can be expressed as:

$$\check{\phi}_l = \phi_l + \Delta\phi_l \quad (67)$$

Then, the solution \tilde{p}_l at measurement $\check{\phi}_l$ is:

$$\tilde{p}_l = \check{p}_l + \Delta p_l = g(\check{\phi}_l + \Delta\phi_l) \quad (68)$$

Expanding (68) in a Taylor series about carrier phase at $\check{\phi}_l$, we have:

$$\tilde{p}_l \approx g(\check{\phi}_l) + \left. \frac{\partial g(\phi_l)}{\partial \phi_l} \right|_{\phi_l = \check{\phi}_l} \Delta\phi_l \quad (69)$$

where $\left. \frac{\partial g(\phi_l)}{\partial \phi_l} \right|_{\phi_l = \check{\phi}_l}$ is:

$$\frac{\partial g(\phi_l)}{\partial \phi_l} = \begin{cases} \frac{\phi_{S,l} - d_{ts}}{\sqrt{(\phi_{S,l} - d_{ts})^2 + h^2}} & p_l \geq d(\eta_l - 1) \\ -\frac{\phi_{S,l} - d_{ts}}{\sqrt{(\phi_{S,l} - d_{ts})^2 + h^2}} & p_l < d(\eta_l - 1) \end{cases} \quad (70)$$

where $\phi_{S,l} = \phi_l + k_l\lambda - \sqrt{\varepsilon_r}d(\eta_l - 1)$ is the equivalent wireless propagation measurement. And the positioning error is expressed as:

$$\Delta p_l = \tilde{p}_l - g(\check{\phi}_l) = \left. \frac{\partial g(\phi_l)}{\partial \phi_l} \right|_{\phi_l = \check{\phi}_l} \Delta\phi_l \quad (71)$$

And the derivative of $\left. \frac{\partial g(\phi_l)}{\partial \phi_l} \right|_{\phi_l = \check{\phi}_l}$ with respect to ϕ_l can be expressed as:

$$\frac{\partial^2 g(\phi_l)}{\partial \phi_l^2} = \begin{cases} \frac{h^2}{[(\phi_{S,l} - d_{ts})^2 + h^2]^{3/2}} & p_l \geq d(\eta_l - 1) \\ -\frac{h^2}{[(\phi_{S,l} - d_{ts})^2 + h^2]^{3/2}} & p_l < d(\eta_l - 1) \end{cases} \quad (72)$$

Therefore, $\left| \left. \frac{\partial g(\phi_l)}{\partial \phi_l} \right|_{\phi_l = \check{\phi}_l} \right|$ increases with $\phi_{S,l}$. As the range of $\phi_{S,l}$ with larger LCX slot spacing is wider, for the same measuring error $\Delta\phi_l$, the positioning error Δp_l increases with larger slot spacing.

C. EKF equations for dual-antenna positioning

The adjusted EKF equations for dual-antenna positioning are as follows.

The state vector ζ_t at time instance t in (32) is expressed as:

$$\zeta_t = [p_t, d_{ts}^{(1)}, d_{ts}^{(2)}, k_{1,t}^{(1)}\lambda, k_{2,t}^{(1)}\lambda, k_{1,t}^{(2)}\lambda, k_{2,t}^{(2)}\lambda]^T \quad (73)$$

The control vector (37) is expressed as:

$$\mathbf{u}_t = \begin{bmatrix} \frac{1}{4} \sum_{l=1}^2 \sum_{s=1}^2 (\eta_{l,t}^{(s)} - \eta_{l,t-1}^{(s)}) d \\ 0 \\ 0 \\ \left\langle d \left(\eta_{1,t}^{(1)} - \eta_{1,t-1}^{(1)} \right) / \lambda \right\rangle \lambda \\ \left\langle d \left(\eta_{2,t}^{(1)} - \eta_{2,t-1}^{(1)} \right) / \lambda \right\rangle \lambda \\ \left\langle d \left(\eta_{1,t}^{(2)} - \eta_{1,t-1}^{(2)} \right) / \lambda \right\rangle \lambda \\ \left\langle d \left(\eta_{2,t}^{(2)} - \eta_{2,t-1}^{(2)} \right) / \lambda \right\rangle \lambda \end{bmatrix} \quad (74)$$

The Jacobian matrix (38) is expressed as:

$$\rho_t(l, s) = \frac{p_t - (\eta_{l,t}^{(s)} - 1)d}{\sqrt{(h^{(s)})^2 + (p_t - (\eta_{l,t}^{(s)} - 1)d)^2}} \quad (75)$$

$$\mathbf{G}_t = \begin{bmatrix} \rho_t(1,1) & 1 & 0 & 0 & 0 & 0 & 0 \\ \rho_t(2,1) & 1 & 0 & 0 & 0 & 0 & 0 \\ \rho_t(1,1) & 1 & 0 & -1 & 0 & 0 & 0 \\ \rho_t(2,1) & 1 & 0 & 0 & -1 & 0 & 0 \\ \rho_t(1,2) & 0 & 1 & 0 & 0 & 0 & 0 \\ \rho_t(2,2) & 0 & 1 & 0 & 0 & 0 & 0 \\ \rho_t(1,2) & 0 & 1 & 0 & 0 & -1 & 0 \\ \rho_t(2,2) & 0 & 1 & 0 & 0 & 0 & -1 \end{bmatrix} \quad (76)$$

The non-integer and integer state elements in (39) are noted as:

$$\hat{\mathbf{a}}_t = [\hat{p}_t, \hat{d}_{ts}^{(1)}, \hat{d}_{ts}^{(2)}]^T \quad (77)$$

$$\hat{\mathbf{b}}_t = [k_{1,t}^{(1)}, k_{2,t}^{(1)}, k_{1,t}^{(2)}, k_{2,t}^{(2)}]^T \quad (78)$$

The upper and lower range of the integer ambiguity (49) and (50) are expressed as:

$$\boldsymbol{\sigma}_\eta = \begin{bmatrix} \eta_{1,t}^{(1)} \\ \eta_{2,t}^{(1)} \\ \eta_{1,t}^{(2)} \\ \eta_{2,t}^{(2)} \end{bmatrix} \quad (79)$$

$$\boldsymbol{\sigma}_h = \begin{bmatrix} h^{(1)} \\ h^{(1)} \\ h^{(2)} \\ h^{(2)} \end{bmatrix} \quad (80)$$

$$\mathbf{k}_{upper} = \left\langle (\sqrt{\varepsilon_r}d(\sigma_\eta - 1) + \sqrt{\sigma_h^2 + \left(\xi \frac{d}{2}\right)^2}) / \lambda \right\rangle \quad (81)$$

$$\mathbf{k}_{lower} = \langle (\sqrt{\varepsilon_r}d(\sigma_\eta - 1) + \sigma_h) / \lambda \rangle \quad (82)$$

D. EKF equations for 2D positioning

The adjusted EKF equations for 2D positioning need to be adjusted to include y direction. The changes are as follows.

The state vector (73) is adjusted to:

$$\zeta_t = [p_{x,t}, p_{y,t}, d_{ts}^{(1)}, d_{ts}^{(2)}, k_{1,t}^{(1)}\lambda, k_{2,t}^{(1)}\lambda, k_{1,t}^{(2)}\lambda, k_{2,t}^{(2)}\lambda]^T \quad (83)$$

The control vector (74) is adjusted to:

$$\mathbf{u}_t = \begin{bmatrix} \frac{1}{4} \sum_{l=1}^2 \sum_{s=1}^2 \left(\eta_{l,t}^{(s)} - \eta_{l,t-1}^{(s)} \right) d \\ 0 \\ 0 \\ 0 \\ \left\langle d \left(\eta_{1,t}^{(1)} - \eta_{1,t-1}^{(1)} \right) / \lambda \right\rangle \lambda \\ \left\langle d \left(\eta_{2,t}^{(1)} - \eta_{2,t-1}^{(1)} \right) / \lambda \right\rangle \lambda \\ \left\langle d \left(\eta_{1,t}^{(2)} - \eta_{1,t-1}^{(2)} \right) / \lambda \right\rangle \lambda \\ \left\langle d \left(\eta_{2,t}^{(2)} - \eta_{2,t-1}^{(2)} \right) / \lambda \right\rangle \lambda \end{bmatrix} \quad (84)$$

(75) is adjusted to:

$$\rho_t(l, s) = \begin{bmatrix} \frac{p_{x,t} - (\eta_{l,t}^{(s)} - 1)d}{\sqrt{(p_{y,t} - p_{LCX}^{(s)})^2 + (p_{x,t} - (\eta_{l,t}^{(s)} - 1)d)^2}} \\ \frac{p_{y,t} - p_{LCX}^{(s)}}{\sqrt{(p_{y,t} - p_{LCX}^{(s)})^2 + (p_{x,t} - (\eta_{l,t}^{(s)} - 1)d)^2}} \end{bmatrix}^T \quad (85)$$

The non-integer state elements (77) is adjusted to:

$$\hat{\mathbf{a}}_t = [\hat{p}_{x,t}, \hat{p}_{y,t}, \hat{d}_{ts}^{(1)}, \hat{d}_{ts}^{(2)}]^T \quad (86)$$

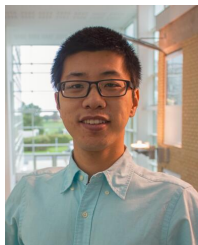
(80) is adjusted to:

$$\sigma_h = \begin{bmatrix} p_{y,t} - p_{LCX}^{(1)} \\ p_{y,t} - p_{LCX}^{(1)} \\ p_{y,t} - p_{LCX}^{(2)} \\ p_{y,t} - p_{LCX}^{(2)} \end{bmatrix} \quad (87)$$

REFERENCES

- [1] Y. Wu, Z. Wei, J. Weng, and H. Deng, "Position manipulation attacks to balise-based train automatic stop control," *IEEE Transactions on Vehicular Technology*, vol. 67, no. 6, pp. 5287–5301, 2018.
- [2] N. Wei, L. Zichao, M. Lanfei, X. Yidan, and L. Xiang, "A comprehensive review on train positioning technique in industries with maglev included based on cross coding inductive loop wire," in *IEEE International Conference on Electronics Information and Emergency Communication*, July 2019, pp. 429–433.
- [3] J. Otegui, A. Bahillo, I. Lopetegui, and L. E. Diez, "Simulation framework for testing train navigation algorithms based on 9-DOF-IMU and tachometers," *IEEE Transactions on Instrumentation and Measurement*, vol. 69, no. 7, pp. 5260–5273, 2019.
- [4] S. Kaiyue, W. Jian, J. Wei, and C. Baigen, "Research on train autonomous positioning method based on long baseline RTK resolution," in *IEEE 25th International Conference on Intelligent Transportation Systems*, October 2022, pp. 329–334.
- [5] L. Yin, Q. Ni, and Z. Deng, "A GNSS/5G integrated positioning methodology in D2D communication networks," *IEEE Journal on Selected Areas in Communications*, vol. 36, no. 2, pp. 351–362, 2018.
- [6] K. Zhang, F. Zhang, G. Zheng, and A. Saleem, "GBSB model for MIMO channel using leaky coaxial cables in tunnel," *IEEE Access*, vol. 7, pp. 67 646 – 67 655, 2019.
- [7] B. Lu, S. Chao, G. D. Andrew, Z. Hongbo, C. Joon, Wayn, and F. Wenquan, "GNSS-5G hybrid positioning based on multi-rate measurements fusion and proactive measurement uncertainty prediction," *IEEE Transactions on Instrumentation and Measurement*, vol. 71, p. 8501415, 2022.
- [8] K. Han, Y. Liu, Z. Deng, L. Yin, and L. Shi, "Direct positioning method of mixed far-field and near-field based on 5G massive MIMO system," *IEEE Access*, vol. 7, pp. 72 170–72 181, 2019.
- [9] Mike, Koivisto, Mario, Costa, Janis, Werner, Kari, Heiska, Jukka, and Talvitie, "Joint device positioning and clock synchronization in 5G ultra-dense networks," *IEEE Transactions on Wireless Communications*, vol. 16, no. 5, pp. 2866–2881, 2017.
- [10] 3GPP, "TS 22.261 v19.0.0: Service requirements for the 5G system," 2022.
- [11] K. Kyeongjun, B. Ilmu, A. Woojin, and S. Wonjae, "High-speed train positioning using deep Kalman filter with 5G NR signals," *IEEE Transactions on Intelligent Transportation Systems*, vol. 23, no. 9, pp. 15 993 – 16 004, 2022.
- [12] M. A. Trivedi and J. H. van Wyk, "Localization and tracking of high-speed trains using compressed sensing based 5G localization algorithms," in *IEEE 24th International Conference on Information Fusion*, November 2021, pp. 1–8.
- [13] J. Talvitie, T. Levanen, M. Koivisto, and M. Valkama, "Positioning and tracking of high-speed trains with non-linear state model for 5G and beyond systems," in *16th International Symposium on Wireless Communication Systems*, August 2019, pp. 309–314.
- [14] J. Zhu, P. Hou, Y. Hou, S. Denno, and M. Okada, "Two-dimensional RSSI-based indoor localization using multiple leaky coaxial cables with a probabilistic neural network," *IEEE ACCESS*, vol. 10, pp. 21 109 – 21 119, 2022.
- [15] J. Engelbrecht, G. Forster, O. Michler, and R. Collmann, "Positioning estimation in public transport systems by leaky coaxial cables," in *Workshop on Positioning Navigation and Communication*, March 2012, pp. 175–179.
- [16] M. Weber, U. Birkel, R. Collmann, J. Engelbrecht, and T. Mittelhessen, "Wireless indoor positioning: Localization improvements with a leaky coaxial cable prototype," pp. 1–3, September 2011.
- [17] K. I. Nishikawa, T. Higashino, K. Tsukamoto, and S. Komaki, "A new position detection method using leaky coaxial cable," *IEICE Electronics Express*, vol. 5, no. 8, pp. 285–290, 2008.
- [18] Nishikawa, K. I. and Higashino, T. and Tsukamoto, K. and Komaki, S., "Two dimensional position detection method using bi-directional leaky coaxial cable based on TDOA," in *IEEE 20th International Symposium on Personal, Indoor and Mobile Radio Communications*, April 2010, pp. 2167–2170.
- [19] K. Shirai, T. Higashino, and M. Okada, "An experimental investigation of the MUSIC-based wireless position location using LCX antenna at 5GHz band," in *International Symposium on Communications and Information Technologies*, September 2019, pp. 118–121.
- [20] T. Higashino and M. Okada, "A wireless sensing technique based on channel estimation in leaky coaxial cable antenna system," in *URSI General Assembly and Scientific Symposium*, August 2014, pp. 309–314.
- [21] X. Li and K. Pahlavan, "Super-resolution TOA estimation with diversity for indoor geolocation," *IEEE transactions on wireless communications*, vol. 3, no. 1, pp. 224–234, 2004.
- [22] J. H. Wang and K. K. Mei, "Theory and analysis of leaky coaxial cables with periodic slots," *IEEE Trans Antennas and Propagation*, vol. 49, no. 12, pp. 1723–1732, 2001.
- [23] S. Lin, J. Wang, S. Hua, and Z. Li, "Research on the radiation characteristics of the leaky coaxial cables," in *International Symposium on Antennas*, March 2003, pp. 242–245.
- [24] Z. Chaloupka, "Technology and standardization gaps for high accuracy positioning in 5G," *IEEE Communications Standards Magazine*, vol. 1, no. 1, pp. 59–65, 2017.
- [25] 3GPP, "TS 38.211 v17.3.0: NR physical channels and modulation," 2022.
- [26] G. Satya, L. Pathak, G. Ponnammareddy, and D. Das, "NRPos: A multi-RACH framework for 5G NR positioning," in *IEEE 3rd 5G World Forum*, September 2020, pp. 25–30.

- [27] J. Zhu, Y. Hou, S. Denno, and M. Okada, "A study for 2-D indoor localization using multiple leaky coaxial cables," *APSIPA Transactions on Signal and Information Processing*, vol. 9, no. 1, pp. 1–8, 2020.
- [28] 3GPP, "TS 37.355 v17.4.0: LTE Positioning Protocol (LPP)," 2022.
- [29] 3GPP, "TS 38.331 v17.4.0: Radio Resource Control (RRC) protocol specification," 2022.
- [30] 3GPP, "TS 38.213 v17.5.0: Physical layer procedures for control," 2023.
- [31] V. Bellad, M. G. Petovello, and G. Lachapelle, "Tracking and position errors in GNSS receivers with intermittent signal tracking," *Navigation: Journal of The Institute of Navigation*, vol. 63, no. 2, pp. 193–204, 2016.
- [32] Bellad, Vijaykumar and Petovello, Mark G. and Lachapelle, Gerard, "Intermittent tracking in weak signal environments," in *2015 International Conference on Indoor Positioning and Indoor Navigation (IPIN)*, 2015, pp. 1–10.
- [33] Y. Liu, Z. Qin, M. ElKashlan, Z. Ding, A. Nallanathan, and L. Hanzo, "Nonorthogonal multiple access for 5G and beyond," *Proceedings of the IEEE*, vol. 105, no. 12, pp. 2347–2381, 2017.
- [34] Z. Song, Y. Liu, and X. Sun, "Joint task offloading and resource allocation for NOMA-enabled multi-access mobile edge computing," *IEEE Transactions on Communications*, vol. 69, no. 3, pp. 1548–1564, 2021.
- [35] Y. Liu, Z. Ding, M. ElKashlan, and H. V. Poor, "Cooperative Non-orthogonal Multiple Access with simultaneous wireless information and power transfer," *IEEE Journal on Selected Areas in Communications*, vol. 34, no. 4, pp. 938–953, 2016.
- [36] E. Kaplan and C. J. Hegarty, *Understanding GPS/GNSS: Principles and Applications, Third Edition*, 3rd ed. USA: Artech House, Inc., 2017.
- [37] X. Cai, X. Yin, X. Cheng, and A. P. Yuste, "An empirical random-cluster model for subway channels based on passive measurements in UMTS," *IEEE Transactions on Communications*, vol. 64, no. 8, pp. 3563–3575, 2016.
- [38] P. Liu, J. Feng, W. Ge, H. Wang, X. Liu, D. Wang, T. Song, and J. Chen, "A system-level performance evaluation for a 5G system under a leaky coaxial cable MIMO channel for high-speed trains in the railway tunnel," *Electronics*, vol. 11, no. 8, p. 1185, 2022.
- [39] F. Yang, X. Zhang, and X. Fan, "Design and simulation analysis of the graded LCX," in *2017 International Conference on Wireless Communications, Signal Processing and Networking (WiSPNET)*. IEEE, 2017, pp. 675–678.
- [40] 3GPP, "TS 38.101 v17.9.0: User Equipment (UE) radio transmission and reception," 2023.
- [41] H. Jiang, T. Li, D. Song, and C. Shi, "An effective integrity monitoring scheme for GNSS/INS/vision integration based on error state EKF model," *IEEE Sensors Journal*, vol. 22, no. 7, pp. 7063–7073, 2022.
- [42] J. Qin and Z. Liu, "Multi-modal sensor fusion method based on Kalman filter," in *2021 IEEE Conference on Telecommunications, Optics and Computer Science (TOCS)*. IEEE, 2021, pp. 515–519.



Lu Yin (M'17) received the B.Sc. and Ph.D degrees in electrical engineering from Beijing University of Posts and Telecommunications (BUPT), Beijing, China, in 2014. He is currently an associate professor with School of Electronic Engineering, BUPT. He was an academic visitor with Lancaster University from 2016 to 2017. His current research interests are in the areas of GNSS, indoor positioning, integrated/cooperative positioning and timing, intelligent localization (localization with artificial intelligence), positioning-communication integration system and communication system. He is now involved in the development and standardization of 3GPP 5G NR positioning.



Tianzhu Song received the B.S. degree from South West Jiaotong University, Chengdu, China, in 2021. He is currently pursuing the Ph.D. degree in the Beijing University of Posts and Telecommunications, Beijing, China. His current research interests are in the areas of wireless positioning and positioning-communication integration systems.



Qiang Ni (M'04–SM'08) is currently a Professor and the Head of the Communication Systems Group, School of Computing and Communications, Lancaster University, Lancaster, U.K. His research interests include the area of future generation communications and networking, including green communications and networking, millimeter-wave wireless communications, cognitive radio network systems, non-orthogonal multiple access (NOMA), heterogeneous networks, 5G and 6G, SDN, cloud networks, energy harvesting, wireless information and power transfer, IoTs, cyber physical systems, AI and machine learning, big data analytics, and vehicular networks. He has authored or co-authored 300+ papers in these areas. He was an IEEE 802.11 Wireless Standard Working Group Voting Member and a contributor to various IEEE wireless standards.



Quanbin Xiao received the B.S. and M.S. degrees from Beijing University of Posts and Telecommunications, Beijing, China, in 2020 and 2023, respectively. His research interests are in the areas of precise point positioning (PPP), real-time kinematic positioning (RTK) and wireless positioning.



Yuan Sun received the B.E. degree from the School of Instrumentation Science and Optoelectronics Engineering, Beihang University, Beijing, China, in 2011, and the Ph.D. degree from the School of Electronic and Information Engineering, Beihang University, in 2016. She is currently an associate professor with the School of Electronics Engineering, Beijing University of Posts and Telecommunications, Beijing. Her primary research interests include global navigation satellite system positioning and integrity monitoring.



Wenfang Guo received the B.S. degree in Electronic and Information Engineering from University of South China, Hengyang, China. She is currently pursuing the M.S. degree with the Beijing University of Posts and Telecommunications, Beijing, China. Her current research interests are in the areas of wireless positioning and protocol for 5G NR positioning.